

**Modeling Depletion-Type Silicon Micro-Ring  
Modulator Considering Its Self-Heating Effect**

*Myungjin Shin*

*(Walter Jin Shin)*

**The Graduate School**

**Yonsei University**

**Department of Electrical and Electronic Engineering**

**Modeling Depletion-Type Silicon Micro-Ring  
Modulator Considering Its Self-Heating Effect**

by

***Myungjin Shin***  
***(Walter Jin Shin)***

Master's Thesis

Submitted to the Department of Electrical and Electronic Engineering  
and the Graduate School of Yonsei University  
in partial fulfillment of the requirements for the degree of

**Master of Science**

**February 2017**

This certifies that the master's thesis of Myungjin Shin is approved.

---

**Thesis Supervisor: Woo-Young Choi**

---

**Sang-Kook Han**

---

**Lars Zimmermann**

**The Graduate School**

**Yonsei University**

**February 2017**

# Table of Contents

<b>Table of Contents</b> .....	i
<b>List of Tables</b> .....	iii
<b>List of Figures</b> .....	iv
<b>Abstract</b> .....	vii
<b>1. Introduction</b> .....	1
1.1. Optical Interconnect .....	1
1.2. Silicon Photonics .....	4
1.3. Optical Modulators in Silicon Photonics .....	8
1.4. Flow of Dissertation .....	14
<b>2. Si Micro-Ring Modulator</b> .....	16
2.1. Ring Resonator .....	18
2.1.1. Round-Trip Approach .....	18
2.1.2. Coupled-Mode Approach .....	24
2.2. Plasma Dispersion Effect .....	28
<b>3. Self-Heating in Depletion-Type Si MRM</b> .....	32
3.1. Influence of Self-Heating .....	32



## List of Tables

<b>Table 1-1.</b> Summary of Si Photonics Foundry Services .....	7
<b>Table 1-2.</b> Summary of State-of-the-art Si Optical Modulators .....	13
<b>Table 3-1.</b> Extracted Si MRM Parameters .....	41
<b>Table 3-2.</b> Extracted Si MRMs Parameters Having Different Radii ....	52
<b>Table 3-3.</b> Extracted Parameters for Si MRMs Having Different Doping Concentration .....	56
<b>Table 4-1.</b> Extracted Parameter Values for $B_{\text{Para}}$ and $B_{\text{Core}}$ .....	75
<b>Table 4-2.</b> Extracted Optical Parameter Values of Si MRM .....	78
<b>Table 4-3.</b> Calculated Corresponding $B_{\text{Opt}}$ Parameters from Table 4-2 .... .....	79
<b>Table 4-4.</b> Calculated Corresponding $B_{\text{Opt}}$ Parameters for Different $V_{\text{signal}}$ at $\lambda_{\text{in}}=1559.546\text{nm}$ .....	92

## List of Figures

<b>Fig. 1-1.</b> Enlargement of application range of optical interconnect.....	3
<b>Fig. 1-2.</b> Monolithically-integrated EPIC on Si wafer .....	6
<b>Fig. 1-3.</b> Structure of Si MZM .....	11
<b>Fig. 1-4.</b> Structure of Ge-on-Si EAM .....	12
<b>Fig. 1-5.</b> Structure of Si MRM .....	12
<b>Fig. 2-1.</b> Structure and parameters of Si ring resonator for round-trip approach.....	20
<b>Fig. 2-2.</b> Transmission characteristic of MRR .....	23
<b>Fig. 2-3.</b> Ring resonator decay-time constants for coupled-mode analysis: (a) round-trip loss ( $\tau_l$ ) and (b) coupling loss ( $\tau_e$ ) ..	27
<b>Fig. 2-4.</b> Structure and transmission characteristics of carrier-injection Si MRM .....	30
<b>Fig. 2-5.</b> (a) Structure and (b) transmission characteristics of depletion-type Si MRM.....	31
<b>Fig. 3-1.</b> Temperature sensitivity of depletion-type Si MRM .....	33
<b>Fig. 3-2.</b> (a) Interaction between optical power and free-carrier. (b) Principle of self-heating .....	34
<b>Fig. 3-3.</b> (a) Chip photo and structure as well as (b) cross-section of Si MRM .....	37
<b>Fig. 3-4.</b> (a) Measured broad transmission spectrum of Si MRM. (b) Measured and calculated transmission spectra without self-	

heating.....	38
<b>Fig. 3-5.</b> Transmission characteristics of Si MRM with five different input optical powers .....	42
<b>Fig. 3-6.</b> (a) Measured resonance wavelength and (b) effective index variation at resonance wavelength for 5 different input optical powers. In addition estimated effective index variation due to only temperature change and dispersion are shown in (b) .....	47
<b>Fig. 3-7.</b> Measured transmission spectra at two different input powers. Asymmetric shape is shown for high input optical power .....	50
<b>Fig. 3-8.</b> Measured and calculated transmission spectra at different input optical powers for Si MRMs having different radii and directional coupler gap distances. (a) 8 $\mu$ m and 290nm), (b) 12 $\mu$ m and 250 nm, and (c) 16 $\mu$ m and 220 nm .....	51
<b>Fig. 3-9.</b> Measured and calculated transmission spectra at different input optical powers for Si MRMs having different doping concentration, (a) 7x10 <sup>17</sup> (cm <sup>-3</sup> ), 5x10 <sup>18</sup> (cm <sup>-3</sup> ) for P-, N-type, (b) 5x10 <sup>17</sup> (cm <sup>-3</sup> ), 3x10 <sup>18</sup> (cm <sup>-3</sup> ) for P-, N-type.....	55
<b>Fig. 4-1.</b> Block diagram of equivalent circuit for Si MRM.....	62
<b>Fig. 4-2.</b> (a) Parasitic components of pads and interconnects, and (b) its equivalent circuit ( $B_{para}$ ). .....	65
<b>Fig. 4-3.</b> (a) Cross section as well as electrical components for Si MRM core, and (b) its equivalent circuit ( $B_{Core}$ ).....	67
<b>Fig. 4-4.</b> Equivalent circuit of Si MRM optical modulation characteristics ( $B_{Opt}$ ) .....	70
<b>Fig. 4-5.</b> Measured (circles) and simulated (colored solid line) S11 of Si MRM .....	74

<b>Fig. 4-6.</b> Experimental setup for parameter extraction of $B_{Opt}$ of Si MRM and frequency response .....	76
<b>Fig. 4-7.</b> Measured and simulated transmission characteristic of Si MRM .....	77
<b>Fig. 4-8.</b> (a) Full equivalent circuit model of Si MRM .....	80
(b) Measured (circles) and simulated (solid line) relative frequency responses at three different detuning levels.....	81
<b>Fig. 4-9.</b> Simulated normalized frequency responses of $B_{para}$ , $B_{para}$ & $B_{Core}$ and $B_{para}$ & $B_{Core}$ & $B_{Opt}$ at three different detuning levels.....	84
<b>Fig. 4-10.</b> (a) Schematic of transmitter used for simulation including driver and Si MRM. (b) Simulated gain-bandwidth product of transmitter with different detuning ( $D$ ) as well as driver load impedance ( $R_L$ ) .....	85
<b>Fig. 4-11.</b> Simulated frequency response of transmitter with (a) three different detuning conditions at $R_L=100\Omega$ and (b) four different $R_L$ at $D=90\text{GHz}$ .....	86
<b>Fig. 4-12.</b> Influence of self-heating in modulation dynamics.....	89
<b>Fig. 4-13.</b> Transmission characteristics for two different optical powers. Same symbols have same normalized transmission output value. (b) Normalized frequency responses for two different input optical powers. Input optical wavelengths are notified in (a).....	90
<b>Fig. 4-14.</b> (a) Simulated and (b) measured eye diagrams for 25-Gb/s PRBS 231-1 pattern at the input wavelength of 1559.546nm .....	93

## **Abstract**

# **Modeling Depletion-Type Silicon Micro-Ring Modulator Considering Its Self-Heating Effect**

*Myungjin Shin*

Dept. of Electrical and Electronic Engineering  
The Graduate School  
Yonsei University

The influences of self-heating on the static transmission characteristics and modulation dynamics of depletion-type Si micro-ring modulators (MRMs) are investigated. Self-heating, caused by free-carrier absorption of the input light inside the doped ring waveguide, increases the effective refractive index of the ring waveguide and

results in the red-shifted resonance wavelength. This phenomenon is modeled based on the coupled-mode equation with a newly-introduced self-heating coefficient,  $R$ . Furthermore, dependence of  $R$  on device size and doping concentration is experimentally investigated the resulting dependence is explained. In addition, based on this parametric characterization, the influence of self-heating in modulation dynamics is also analyzed.

Moreover, in this dissertation, a linear equivalent circuit model for the depletion-type Si MRM is presented. Equivalent circuit model consists of three blocks: one for parasitic components due to interconnects and pads, another for the electrical elements of the core PN junction, and the third for a lossy LC tank that models optical modulation characteristics of Si MRM. Simulated modulation characteristics with our equivalent circuit show very good agreement with measured results for small-signal modulation frequency responses and large-signal eye diagrams.

Using this model, we can analyze characteristics of Si MRM modulation frequency response and perform design optimization of the entire Si photonic transmitter consisted of a Si MRM and electrical driver circuits. The accuracy of each suggested model is confirmed with the measurement results.

---

**Keywords:** Silicon photonics, optical interconnect, Si micro-ring modulator, self-heating, self-heating coefficient, equivalent circuit model.

# **1. Introduction**

## **1.1. Optical Interconnect**

In data transmission, interconnection always has been one of the most critical issues since it determines the performance of whole system. Based on its domain, interconnection can be categorized into two different types, electrical interconnection and optical interconnection, and both technologies have always been competed to be the solution of choice. Each offers specific tradeoffs based on density, reach, reliability, cost in a given application. With their characteristics, historically, electrical interconnections have been widely used in short-distance application as they have advantages on cost efficiency and compatibility with integrated circuit. On the other hand, optical interconnections have been used for long-distance application as they have advantages on large bandwidth, low loss and, its immunity to electro-magnetic interference (EMI).

In recent years, since the demand of data capacity increases dramatically with the huge success of smartphones and an advent of data center, electrical interconnections start to become main obstacle for required speed called ‘interconnect bottleneck’. Therefore, in order to meet the speed and data capacity requirements, electrical

interconnects in short-distance application have been replaced by optical interconnects, such as optical fiber [1], and, thus, the application range of the optical interconnects have been enlarged to the shorter-distance application shown in Fig. 1-1 [2].

In order to be used for shorter-distance applications, however, a number of photonic components should be fabricated into single chip, and it is not possible for III-V compound based optics to compete with Si electronics in the aspect of cost and productivity, since the mass production of fabrication technology for III-V materials is far behind those for Si electronics [3]. In this regard, Si-based optical interconnects, Si photonics, are attracting a great amount of research and development efforts in recent years.

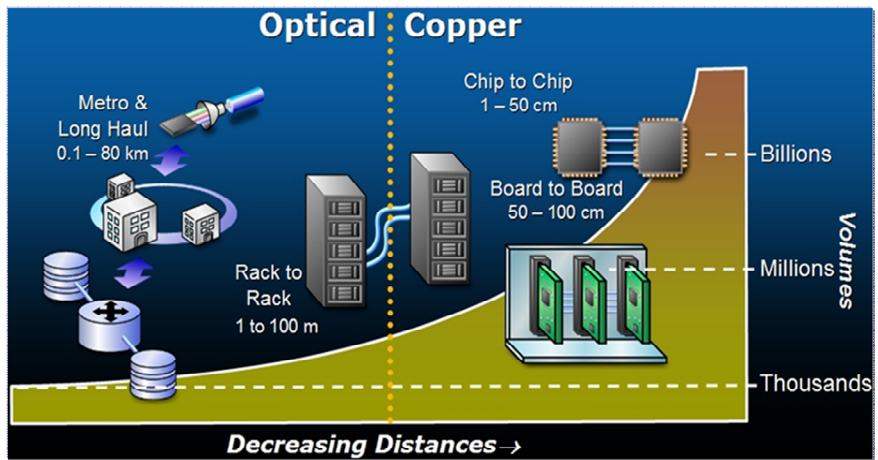


Fig. 1-1. Enlargement of application range of optical interconnect [1].

## **1.2. Silicon Photonics**

Si photonics attract great amount of research and development efforts ranging from rack-to-rack, board-to-board, and chip-to-chip optical interconnects. The most intriguing merit for Si photonics is mainly based on reusing the conventional complementary metal-oxide-semiconductor (CMOS) fabrication infrastructures and the development of photonic integrated circuits (PICs) based on SOI that enable high-bandwidth, cost-effective, and small-footprint optical interconnect systems [4], [5]. And these advantages will lead to the development of monolithic electronic-photonic integrated circuits (EPICs) based on both CMOS and BiCMOS technology [6], [7] as illustrated in Fig. 1-2 [8].

However, despite of its advantages, due to several drawbacks, Si photonics has not been briskly used to practical applications yet. For example, even though Si may be the perfect material for realizing optical waveguides with its high confinement factor, it is not suitable for active photonic devices such as photodetectors or lasers due to its physical characteristics [9]. Therefore, they always need an additional light source and detector to realize the full optical link which accompanies additional cost for packaging. Moreover, existing Si processing technologies needs additional modification for photonic

components to be implemented [10]. Recently, with the profound effort of many industries and academics, Si photonics foundry is now allowed at reasonable cost and this phenomenon is changing the paradigm in the photonics research area. Based on this phenomenon, there are several commercially available Si photonics foundry services summarized in Table 1-1[11, 12, 13]. Following this trend, many researchers including myself are expecting for Si photonic to be dramatically accelerated.

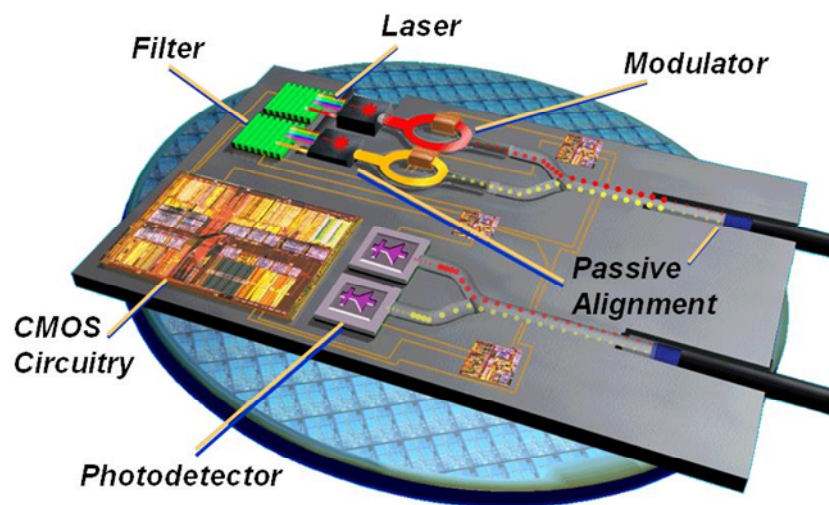


Fig. 1-2. Monolithically-integrated EPIC on Si wafer [8].

TABLE 1-1  
SUMMARY OF SI PHOTONICS FOUNDRY SERVICES

	<b>IME</b>	<b>IMEC</b>	<b>CEA- LETI</b>	<b>IHP</b>
<b>Lithography</b>	248 nm	193 nm	193 nm	248 nm
<b>Wafer size</b>	200 mm	200 mm	200 mm	200 mm
<b>SOI etch depth</b>	60, 130, 220 nm	70, 130, 220 nm	70, 130, 220 nm	70, 120, 220 nm
<b># of doping levels</b>	3	3	2	3
<b># of metal layers</b>	2	1		5
<b>Photodetector</b>	Ge vertical <i>pn</i>	Ge vertical <i>pin</i>	Ge vertical <i>pn</i>	Ge vertical <i>pin</i>
<b>Modulator</b>	Si MZ, Si Ring	Si MZ, Si Ring	Si MZ	Si MZ
<b>Electronics</b>				0.25 $\mu$ m BiCMOS

### **1.3. Optical Modulators in Silicon Photonics**

In optical communication system, optical source can be modulated either directly or externally as each way has its own pros and cons. First, the direct modulation has its strong point in compactness and cost efficiency but mostly it suffers from high noise and low bandwidth due to frequency chirp and limited extinction ratio [14]. On the other hand, external modulation avoids frequency chirp, since it uses additional modulator and, therefore, it achieves larger bandwidth and higher extinction-ratio [15].

In silicon photonics, however, since it has indirect bandgap, it is not proper material to make light source. Therefore, without practical Si lasers, external modulators are always of great interest [16, 17] such as, Mach-Zehnder interferometer (MZI) modulator, or MZM, micro-ring modulator (MRM), and electro-absorption modulators (EAMs). The most widely used optical modulator is MZMs, shown in Fig. 1-3 which use phase difference between two arms to change output optical intensity. These structures have been profoundly investigated with different material, LiNbO<sub>3</sub> or other III-V compound semiconductors. However, since silicon has weak electro-optic effects, the performance of Si MZMs are far behind compare to other MZMs with different

materials, thus, having large footprint, around several millimeters, to meet the required performance. But, based on its big size, they have large electrical parasitic components and require higher driving voltage to get sufficient modulation efficiency. For EAM, shown in Fig. 1-4 [18], high speed Ge-on-Si EAMs have been successfully developed operating with low power in recent study. However, even though Ge EAMs are competitive with those performances, since it is started to be studied in recent days, there are several unknown factors and they still need additional study to be done. In addition, they require extra epitaxial growth steps for additional material which is critical limitation for Ge-on-Si EAMs. Lastly, Si MRM, shown in Fig. 1-5, since they are using resonant structure, have their advantages in several characteristics such as high-bandwidth, small-footprint, cost-effective and actively investigated for the past years. However, despite the advantages of MRM, it has not been widely employed to practical application because of temperature and wavelength sensitivity. Due to its weakness, it always needs additional controller as temperature sensor and heater for tuning purpose which will lead to significant amount of power consumption and area ineffectiveness [19, 20]. Table 1-2 shows the performance of the state-of art Si optical modulators including Ge EAM, Si MZM and Si MRM [21, 22, 23].

However, if we can model the characteristic variation of Si MRM for different thermal condition and compensate its temperature sensitivity, Si MRM can be one of most competitive modulator in Si photonic. Regarding this point, we have model the characteristics of Si MRM considering its self-heating effect which can be critical issue in data modulation. Self-heating, one of the thermal factors in Si MRM, is parametrically characterized in both steady state condition and modulation dynamic condition by suggesting self-heating coefficient ( $R$ ). Furthermore, to be easily utilized with electronic circuit driver for designing optimal Si photonic transmitter, Si MRM's equivalent circuit is also studied.

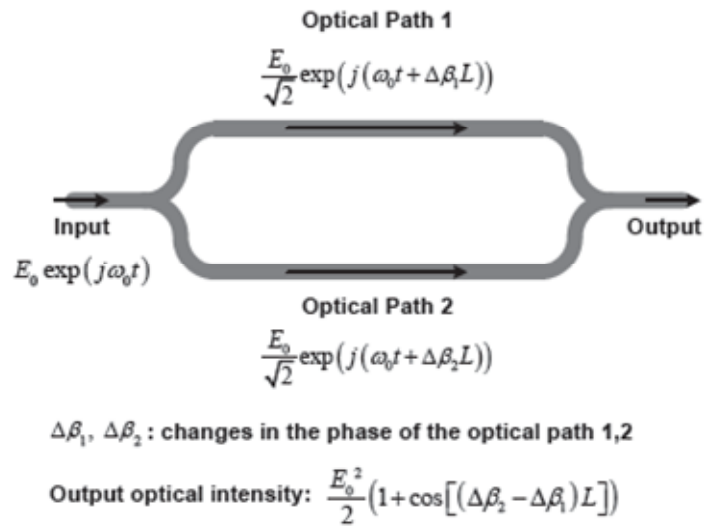


Fig. 1-3. Structure of Si MZM.

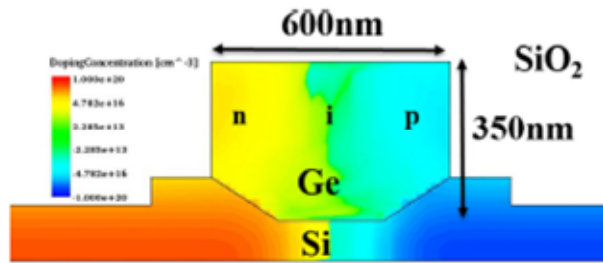


Fig. 1-4. Structure of Ge-on-Si EAM [18]

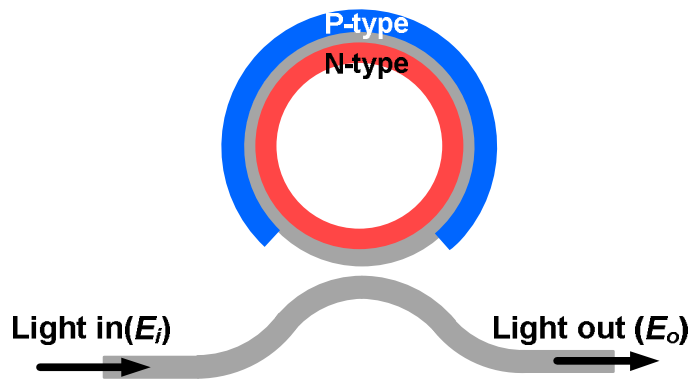


Fig.1-5. Structure of Si MRM

TABLE 1-2  
SUMMARY OF STATE-OF-THE-ART SI OPTICAL MODULATORS

	<b>Ge EAM</b> [21]	<b>Si MZM</b> [22]	<b>Si MRM</b> [23]
<b>Footprint</b> [ $\mu\text{m}^2$ ]	~40 x 10	~3000 x 500	~10 x 10
<b>Wavelength</b> [nm]	1610	1300	1550
<b>Driving voltage</b> [V]	2.0	2.2	1.5
<b>Extinction ratio</b>	3.3	3.4	3.0
<b>Energy efficiency</b> [fJ/bit]	10	450	9
<b>3-dB EO bandwidth</b> [GHz]	>50	30	25
<b>Maximum data rate</b> [Gb/s]	56	50	44

## **1.4. Flow of Dissertation**

This dissertation focuses on analyzing and parametrically characterizing the self-heating in depletion-type Si MRM and modeling easy-to-use equivalent circuit. This characterization of self-heating in Si MRM provides knowledge to understand its characteristics for each input optical powers not only in steady-state condition but also in modulation dynamics. For equivalent circuit model, we are expecting that knowledge from the well-established circuit theory can be easily utilized for intuitive understanding of Si MRM modulation dynamics. The device of interest is focused on depletion-type Si MRM, suitable for high-speed application, but some of them can be expanded to carrier-injection Si MRM. This dissertation is organized in the following manners:

Chapter 2 introduces basic knowledge of Si MRM such as structure, operation principle and accurate behavior model. Since the Si MRM is based on the ring resonator, the operation principle and its behavior model are preferentially introduced. The behavior model is based on coupled-mode theory, a conventional method of describing resonance characteristics. In addition, plasma dispersion effect is introduced as a effective way to modulate effective refractive index in Si platform. With

the knowledge of ring resonator and plasma dispersion effect, the Si MRM can be instinctively understood. In chapter 3, we introduce the influence of self-heating in depletion-type Si MRM in two different characteristics, resonance wavelength shift and asymmetric shape of transfer curve. Both characteristics are parametrically characterized with the introduction of self-heating coefficient ( $R$ ) and the optical power ratio between each wavelength in the ring waveguide. The dependencies on  $R$  based on device structure and doping concentration are also profoundly analyzed. In chapter 4, both small-signal model and large signal model of Si MRM including the influence of self-heating is studied based on the coupled-mode theory. Furthermore, equivalent circuit model, based on lossy LC tank, for small signal model is suggested which can be easily utilized for intuitive understanding of Si MRM modulation dynamics. In addition, such a model should be of great use for designing the optimal Si photonic transmitters that include both Si MRMs and driver electronic circuits. Finally, chapter 5 concludes this dissertation. The accuracy of suggested model is confirmed with the measurement results.

## **2. Si Micro-Ring Modulator**

In Si electro-optic (EO) modulators, free-carrier plasma dispersion effect is one of the most commonly used methods to modulate optical signal by electrical signal. To be specific, electrical signal applied on P-I-N or P-N junction embedded in the waveguide changes the free-carrier concentration for both P-type and N-type causing variation of refractive index [24].

There are two types of Si EO modulators based on this plasma dispersion effect: Si MZMs and Si MRMs. As mentioned above, Si MZMs are based on optical interferometer structures and have advantages of high-speed and stable operation. However, their large footprints have always been the critical weakness following its application. On the other hands, due to resonance characteristics based on optical micro-ring resonator structure, Si MRMs have absolutely small size and low power consumption. Therefore, as mentioned above, even though there are some challenging issues for Si MRMs, it is still one of the promising Si modulators in Si photonics and many researchers are suggesting several ways to compensate their weakness. Regarding this point, modeling and analyzing Si MRM's behavior for several situations can be one of the ways to overcome its weakness.

Following this trend, we have concentrated on modeling depletion-type Si MRM which provides large bandwidth and high modulation efficiency with a small size and low power consumption.

## 2.1. Ring Resonator

### 2.1.1. Round-Trip Approach

Fig. 2-1 shows the structure of the micro ring resonator (MRR) which is basic structure of Si MRM. The ring resonator is composed of one bus waveguide and one ring waveguide. Input light in the bus waveguide partially couple into the ring waveguide experiencing the  $90^\circ$  phase shift and circulate in the ring waveguide.

The optical field in the ring waveguide experience loss and phase shift for every round-trip while circulating in the ring waveguide, represented as  $\alpha$ ,  $\theta$ , respectively.

$$\alpha = \exp(-aL / 2) \text{ and } \theta = \frac{2\pi n_{eff}}{\lambda} L. \quad (2.1)$$

$\alpha$  represents the round-trip loss that optical field experience for each circulation in the ring waveguide and  $a$  represents attenuation constant,  $\theta$ ,  $L$ ,  $n_{eff}$  and  $\lambda$  indicate phase, circumference, effective refractive index of the ring waveguide, and input wavelength, respectively. After circulating in the ring waveguide, some portion of circulating light couples back to bus waveguide. The output optical field amplitude  $E_o$  can be represented by the summation of optical fields that experience different amount of phased shift and loss based on the number of circulation in infinite geometrical progression form.

$$E_o = \gamma E_i - \kappa^2 \alpha \exp(-j\theta) E_i - \kappa^2 \gamma (\alpha \exp(-j\theta))^2 E_i - \dots \quad (2.2)$$

$E_i$  indicates input optical field,  $\gamma$  represents through coefficient, showing amount of optical fields not coupling into the other waveguide in directional coupler,  $\kappa$  is coupling coefficient, representing the amount of optical field coupled into other waveguide. At directional coupler the  $90^\circ$  phase shift is represented as  $-j\kappa$ . With the assumption that other losses are negligible while coupling between ring and bus waveguide,  $\gamma^2 + \kappa^2 = 1$ . These parameters are graphically represented in Fig. 2-1.

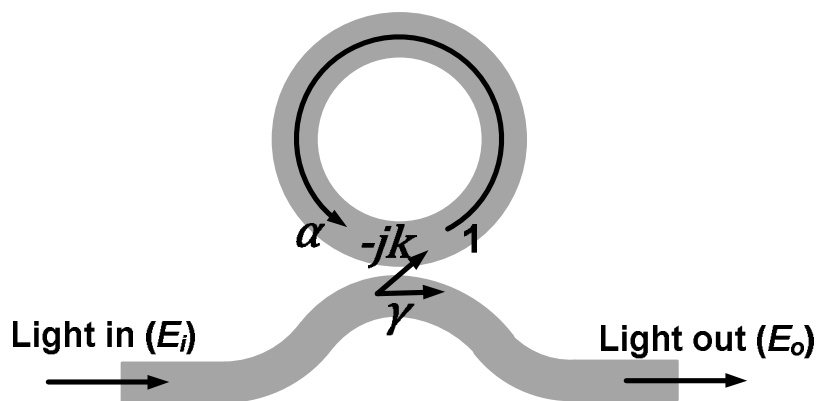


Fig. 2-1. Structure and parameters of Si ring resonator for round-trip approach.

From Eq. (2.2), the optical power transmission  $T$  can be derived as

$$T = \left| \frac{E_o}{E_i} \right|^2 = \frac{\alpha^2 + \gamma^2 - 2\alpha\gamma \cos \theta}{1 + \alpha^2\gamma^2 - 2\alpha\gamma \cos \theta}, \quad (2.3)$$

shown in Fig. 2-2. The wavelength that has in-phase condition ( $\theta=2\pi m$ ) becomes the resonance wavelength of the ring waveguide. The integer term  $m$  is the mode number, representing the number of standing waves in the ring waveguide for one round-trip. Consequently, the condition of resonance wavelength can be represented as

$$m\lambda_{res} = n_{eff}L, \text{ where } m = 1, 2, 3 \dots \quad (2.4)$$

The term  $\lambda_{res}$ ,  $n_{eff}$ , and  $L$  are resonance wavelength, effective refractive index, and ring circumference, respectively. Therefore, at resonance wavelength,  $exp(-j\theta)=1$ , the output optical power  $T$  becomes

$$T = \frac{(\alpha - \gamma)^2}{(1 - \alpha\gamma)^2}. \quad (2.5)$$

Based on Eq. (2.5), when  $\alpha = \gamma$ , the output optical power becomes zero which is called critical coupling. To be specific, this condition comes from when the one round-trip optical power loss in the ring ( $1 - \alpha^2$ ) is equal to the coupling power ( $\kappa^2$ ). The other cases  $\alpha < \gamma$  and  $\alpha > \gamma$  are called under-coupling and over-coupling, respectively.

There are several parameters that describe the characteristics of MRR which are shown in Fig.2-2. First, free spectral range (FSR) is the interval between resonances represented as

$$FSR = \lambda_m - \lambda_{m+1} \approx \frac{\lambda^2}{\eta_g L}, \quad (2.6)$$

where the  $n_g$  represents the group index,  $n_g = n_{eff} - \lambda \frac{dn_{eff}}{d\lambda}$ .

Next term is full width at half maximum (FWHM) of the transmission curve given as

$$FWHM = \frac{(1 - \alpha\gamma)\lambda_{res}^2}{\pi\eta_g L\sqrt{\alpha\gamma}}. \quad (2.7)$$

Finally, the quality factor (Q-factor) shows the sharpness of the resonance defined by

$$Q\text{-factor} = \frac{\lambda_{res}}{FWHM} = \frac{\pi\eta_g L\sqrt{\alpha\gamma}}{(1 - \alpha\gamma)\lambda_{res}}. \quad (2.8).$$

The physical meaning of the Q-factor represents the number of oscillation of the field before circulating energy is depleted to  $1/e$  of the initial energy. From this point of view, it is understood that round trip losses as well as coupling in the directional couplers are loss factors that need to be reduced to obtain high-Q resonances. This Q-factor is directly related to transient response of MRR which will be reconsidered in the later section.

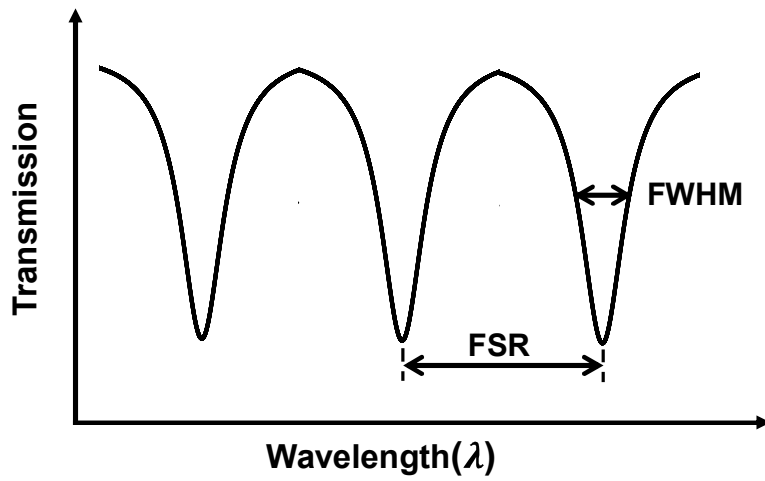


Fig. 2-2. Transmission characteristic of MRR.

### 2.1.2. Coupled-Mode Approach

There is another simple way to describe the characteristics of MRR called coupled-mode approach [25, 26]. By assuming the ring resonator as ideal lossless lumped resonator having  $\omega_{res}$  as resonance angular frequency, the energy amplitude in the ring resonator,  $a(t)$ , can be represented as following equation,

$$\frac{d}{dt}a(t) = j\omega_o a(t). \quad (2.9)$$

Based on Eq. (2.9) ring resonator, when MRR have external bus waveguide with input optical field  $E_i(t)$  considering round-trip and coupling loss, the Eq. (2.9) can be rewritten as

$$\frac{d}{dt}a(t) = (j\omega_{res} - \frac{1}{\tau})a(t) - j\mu E_i(t), \quad (2.10)$$

$$E_o(t) = E_i(t) - j\mu a(t). \quad (2.11)$$

In the above equation,  $\tau$  is the decay time constant for  $a(t)$ , and  $\mu$  represents the change in  $a(t)$  due to the input optical field. Each parameter is shown in the Fig.2-3.

While assuming  $E_i(t)$  having  $exp(j\omega t)$  dependence, we can obtain the steady-state solution for  $a(j\omega)$  as

$$a(j\omega) = \frac{-j\mu}{j(\omega - \omega_{res}) + \frac{1}{\tau}} E_i. \quad (2.12)$$

By substituting Eq. (2.12) into Eq. (2.11), the output optical field and

optical power can be represented as [26]

$$\frac{E_o(t)}{E_i(t)} = \frac{j(\omega - \omega_{res}) + \frac{1}{\tau_l} - \frac{1}{\tau_e}}{j(\omega - \omega_{res}) + \frac{1}{\tau_l} + \frac{1}{\tau_e}}, \quad (2.13)$$

$$T = \left| \frac{E_o(t)}{E_i(t)} \right| = \frac{(\omega - \omega_{res})^2 + \left(\frac{1}{\tau_l} - \frac{1}{\tau_e}\right)^2}{(\omega - \omega_{res})^2 + \left(\frac{1}{\tau_l} + \frac{1}{\tau_e}\right)^2}. \quad (2.14)$$

When input optical wavelength is resonance wavelength ( $\omega = \omega_{res}$ ),

$$T = \frac{\left(\frac{1}{\tau_l} - \frac{1}{\tau_e}\right)^2}{\left(\frac{1}{\tau_l} + \frac{1}{\tau_e}\right)^2}. \quad (2.15)$$

Similar to the round-trip approach, in critical coupling condition ( $1/\tau_e = 1/\tau_l$ ), no optical power is transmitted at the resonance input. With the knowledge of round-trip approach and coupled-mode approach, the relationship between parameters in both round-trip approach ( $\alpha, \gamma$ ) and coupled-mode approach ( $\tau_e, \tau_l$ ) can be represented as following manner,

$$\frac{1}{\tau} = \frac{(2 - \alpha^2 - \gamma^2)c}{2nL}, \quad (2.16)$$

$$\mu^2 = \frac{(1 - \gamma^2)c}{nL}. \quad (2.17)$$

However, it should be noticed that since the coupled-mode approach is based on low loss assumption, coupled mode approach and round-trip approach have similar transmission characteristics only for large  $\alpha, \gamma$ , in other words, where loss is small. When loss gets bigger,

the coupled-mode becomes more erroneous since the assumption of coupled-mode approach, loss in MRM is negligible, becomes flawed. In this dissertation, since the devices researched for the study has low loss, coupled-mode approach and round-trip approach will be used simultaneously.

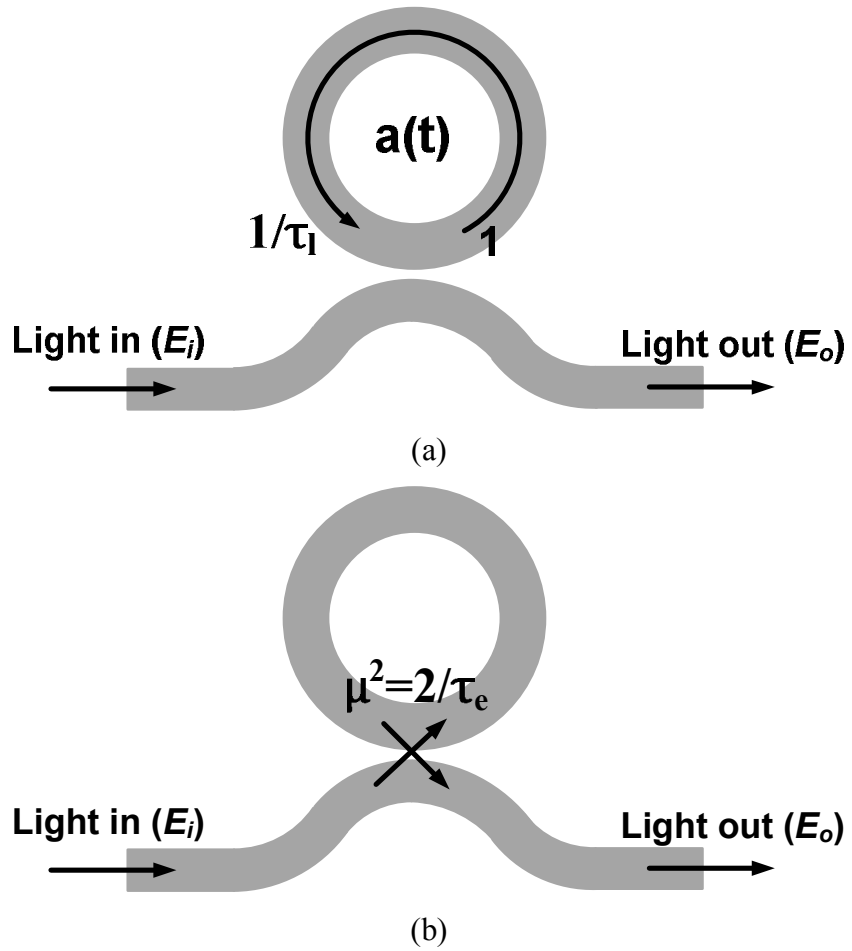


Fig. 2-3. Ring resonator decay-time constants for coupled-mode analysis: (a) round-trip loss ( $\tau_l$ ) and (b) coupling loss ( $\tau_e$ ).

## 2.2. Plasma Dispersion Effect

As mentioned above, applied electric field may change real part ( $\Delta n$ ) and imaginary part ( $\Delta k$ ) of effective refractive index which are Pockels effect, Kerr effect and the Franz–Keldysh effect. These effects result in either the variation of effective refractive index or absorption loss by changing real part ( $\Delta n$ ) or imaginary part ( $\Delta k$ ) of the effective refractive index, respectively. Unfortunately, these electric field effects are weak in silicon at the 1550-nm wavelength which usually used for optical communication [27]. Regarding this point, plasma dispersion effect can be used for excellent alternative method to achieve high-speed modulation [24]. The free-carrier concentration in silicon waveguide can be changed by either injecting or removing carriers in the waveguide. The amount of variation of effective refractive index and the loss at 1550-nm wavelength can be represented as

$$\Delta n = -5.4 \times 10^{-22} \Delta N^{1.011} - 1.53 \times 10^{-18} \Delta P^{0.838}, \quad (2.18)$$

$$\Delta k = 8.88 \times 10^{-21} \Delta N^{1.167} + 5.84 \times 10^{-20} \Delta P^{1.109}, \quad (2.19)$$

where  $\Delta N$  and  $\Delta P$  represents variation of free-carrier concentration for electrons and holes, respectively.

Based on Eq. (2.18), there are two typical ways to change the effective refractive index such as, carrier injection and depletion-type.

Carrier injection type Si MRM, shown in Fig. 2-4 [28], in order to maximize the efficiency of Si MRM, is embedded p-i-n junction in the waveguide and apply forward bias where transmission curve shift to the left. The predominant advantage of carrier-injection Si MRM is high modulation efficiency, and low power consumption. However, since it relies on the slow diffusion minority carriers, its speed is limited. On the other hand, depletion-type Si MRM, shown in Fig. 2-5 [29], using pn junction with reverse bias, has much higher speed. However, since the interaction between optical field and carrier concentration is much less than carrier-injection, the amount of effective refractive index variation is much smaller. Shown in Fig. 2-5 (b), since the depletion-width of the Si MRM increases with the higher bias voltage, the effective refractive index of the ring waveguide increases which results in red-shift of resonance wavelength. Therefore, since depletion-type Si MRM is much suitable for high-speed operation which meets our interest, in this study, we focus on depletion-type Si MRM.

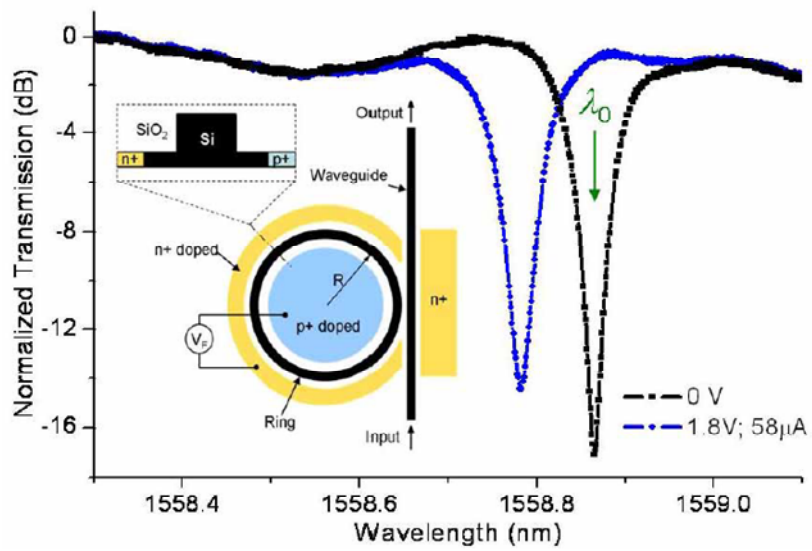
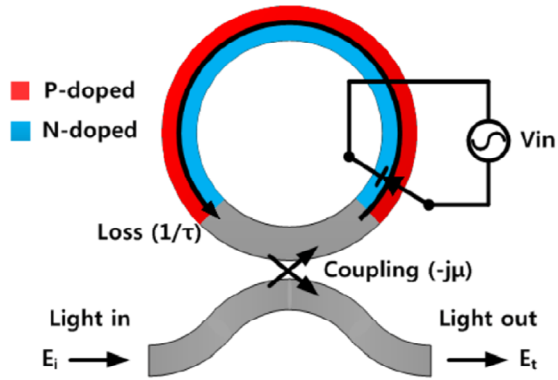
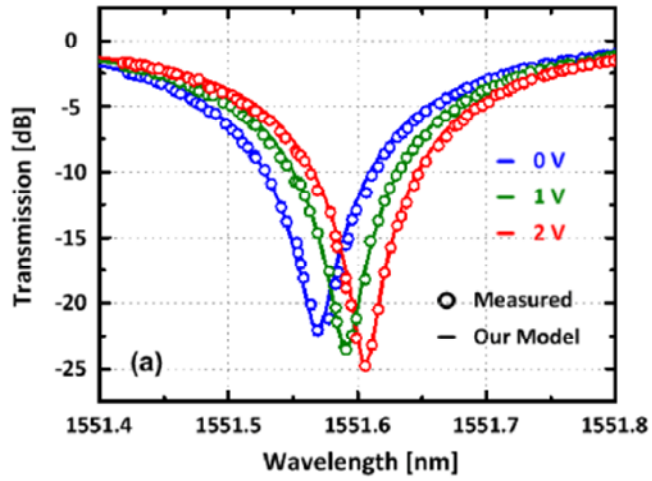


Fig. 2-4. Structure and transmission characteristics of carrier-injection Si MRM [28].



(a)



(b)

Fig. 2-5. (a) Structure and (b) transmission characteristics of depletion-type Si MRM [29].

### **3. Self-Heating in Depletion-Type Si MRM**

#### **3.1. Influence of Self-Heating in Si MRM**

As mention in the previous section, since silicon has high thermo-optic coefficient ( $1.86 \times 10^{-4} \text{ K}^{-1}$ ), one of the most critical weaknesses for depletion-type Si MRM is temperature sensitivity [30, 31]. To verify the sensitivity of our fabricated Si MRM, we measured one of our Si MRMs' the resonance wavelength by changing the external temperature with temperature controller shown in Fig. 3-1. As you can see, in this case, the amount of resonance wavelength shift is about  $70 \text{ pm}/^\circ\text{C}$  which is very critical to data modulation which should be considered and controlled. In particular, self-heating effect is one another factor that influences the temperature condition of Si MRM. Self-heating in Si MRM is caused by free-carrier absorption (FCA) in the ring waveguide. When input optical power couple into the ring waveguide, it interacts with free-carrier in pn-junction embedded in the ring waveguide shown in Fig. 3-2 (a). In succession, the photon energy transfers to the free-carriers, electrons and holes, making them to become excited state. Consequentially, the excited free-carriers return to ground state emanating phonon which heats up the temperature in the ring waveguide shown in Fig. 3-2(b).

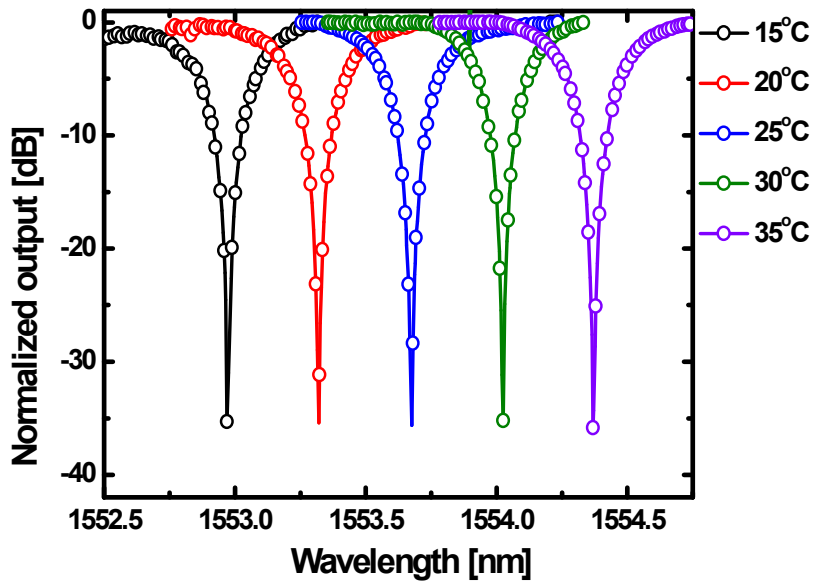
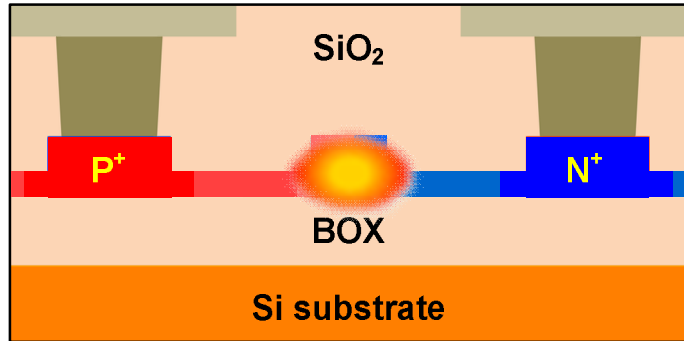
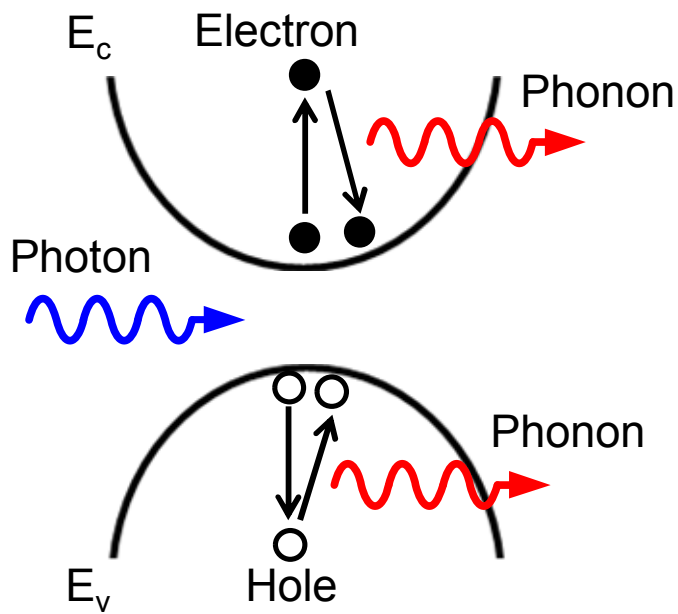


Fig. 3-1. Temperature sensitivity of depletion-type Si MRM.



(a)



(b)

Fig. 3-2. (a) Interaction between optical power and free-carrier. (b) Principle of self-heating.

To visually confirm the influence of self-heating in depletion-type Si MRM, we have measured transmission characteristics of our fabricated Si MRM with different input optical power. Fig. 3-3 (a) shows structure and the chip photo of fabricated Si MRM. As shown in Fig. 3-3(b), the device has 220nm thick Si waveguide above 2 $\mu$ m thick buried oxide (BOX) layer and 500 nm wide ring and bus waveguides. The nominal ratio for N- and P-region widths is 2:3. All Si MRMs reported in this paper were fabricated through Si PIC MPW provided by IHP and have the same device structures except the ring radius, gap distance between ring and bus waveguides, and doping concentration.

Fig. 3-4(a) and (b) show measured transmission spectra for a sample Si MRM. The Si MRM device whose transmission spectrum is shown in Fig. 3-4 has ring radius of 8 $\mu$ m, gap distance of 290 nm and nominal doping concentrations of  $7 \times 10^{17}$  (cm<sup>-3</sup>) for P-region and  $5 \times 10^{18}$  (cm<sup>-3</sup>) for N-region. An Er-doped fiber amplifier is used for the broadband transmission spectrum shown in Fig. 3-4(a), and a tunable laser for the narrow-band spectrum, resonance inside the circle in Fig. 3-4 (a), shown Fig. 3-4(b). The input optical power is reduced as much as possible in order to avoid any self-heating for these measurements. For the spectrum shown in Fig. 3-4(b), the optical power injected into the bus waveguide is estimated 0.025mW after the coupling loss due to

on-chip grating couplers are calibrated out. Si MRM devices are placed on the probing stage whose temperature is actively controlled to be at 25°C.

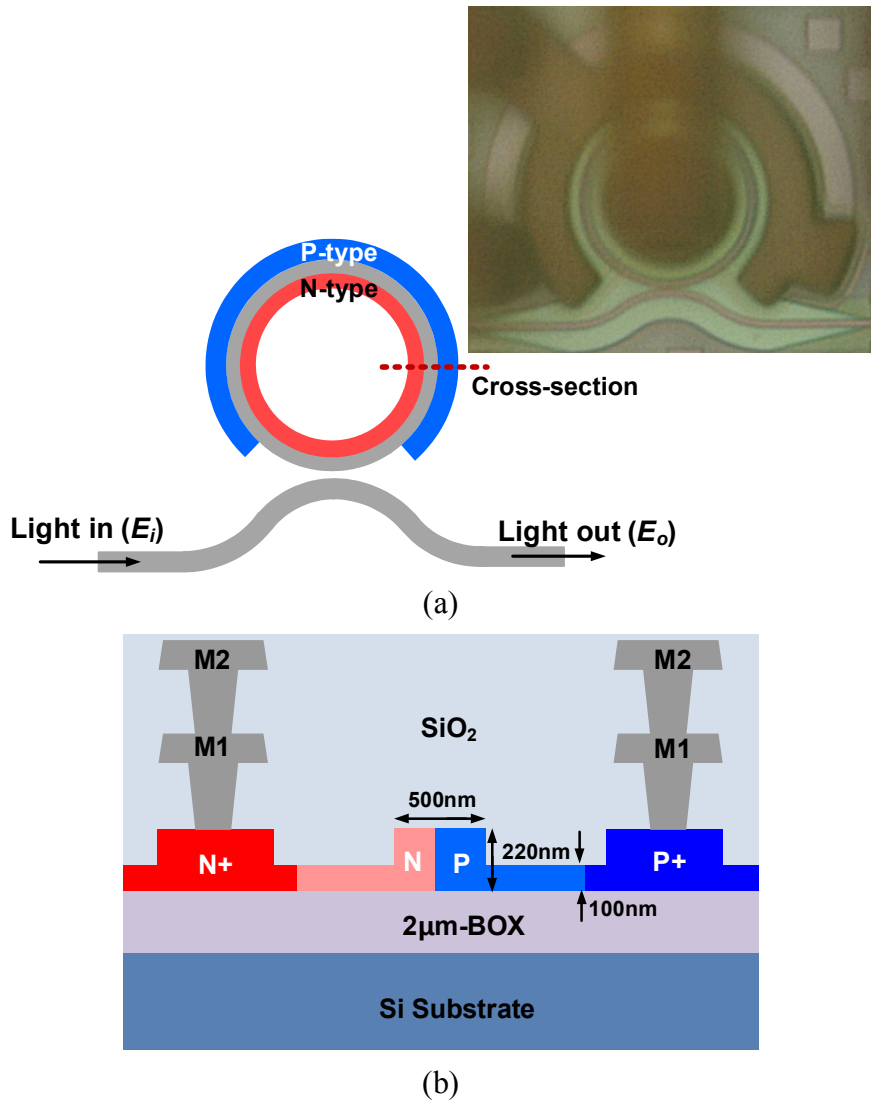
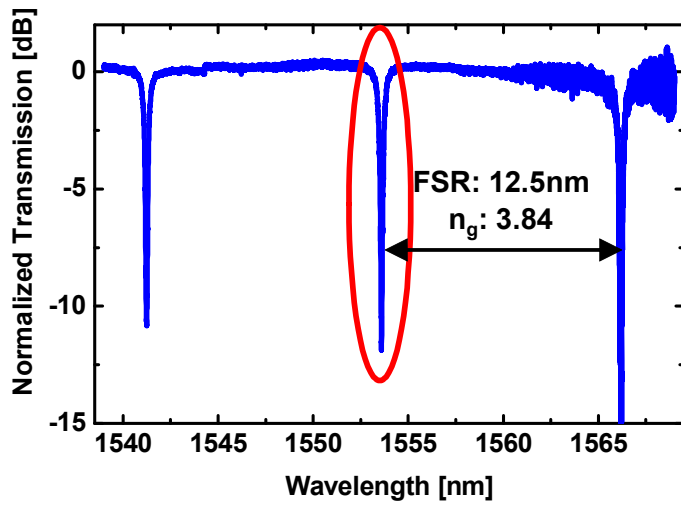
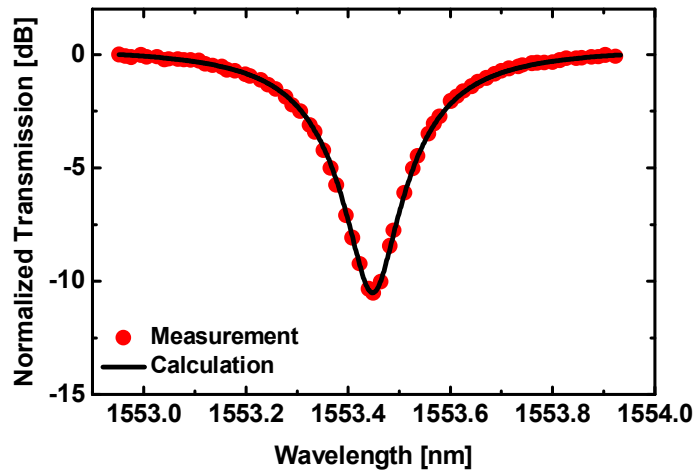


Fig. 3-3. (a) Chip photo and structure as well as (b) cross-section of Si MRM.



(a)



(b)

Fig. 3-4. (a) Measured broad transmission spectrum of Si MRM. (b) Measured and calculated transmission spectra without self-heating. For calculation, extracted parameters given in Table 3-1 are used.

The transmission spectrum in Fig. 3-4(a) shows FSR of 12.5 nm, from which  $n_g$ , the group index, of 3.84 can be determined. Fig. 3-4(b) shows the measured (red circles) narrow-band transmission spectrum for one of the resonance peaks shown in Fig. 3-4(a) along with the calculated results (black line) using the extracted coupled-mode equation parameters. While extracting the parameters, the  $m$  which is integer value, representing the resonance mode number is determined from the numerical simulation of the ring waveguide and  $n_{res}$  is determined from the measured  $\lambda_{res}$  using  $m\lambda_{res}=n_{res}L$ . Then,  $\tau$  and  $u$  are determined by fitting Eq. (2.14) into the measured spectrum so that the minimum mean squared error is achieved. Fig. 3-4(b) shows that measurement and calculation results agree very well. Table 3-1 shows the extracted values for the coupled-mode equation parameters and converted round-trip model parameters for selected resonance peak based on Eq. (2.16) and Eq. (2.17). Although extraction is done for  $\tau$  and  $u$ ,  $\alpha$  and  $\gamma$  are also used in this paper since they are more closely related to the device parameters and allow easier interpretation.

Based on its resonance characteristic, there are different amount of optical power in the ring waveguide with different wavelength and, therefore, the amount of self-heating is different as a function of wavelength. Fig. 3-5 shows the 5 different transmission characteristics

for different input optical power with identical Si MRM. As you can see, there are two different characteristics that should be considered, resonance wavelength shift and asymmetric shape of transfer curve. Therefore, in this chapter, each of them will be modeled separately in following chapters.

TABLE 3-1  
EXTRACTED Si MRM PARAMETERS

$\lambda_{\text{res}}$ (nm)	1553.449
<b>M</b>	86
$n_{\text{res}}$	2.657814
$1/\tau$ (s <sup>-1</sup> ) (x10 <sup>11</sup> )	1.1351
$u^2$ (s <sup>-1</sup> ) (x10 <sup>10</sup> )	8.0938
$\alpha$	0.9669
$\gamma$	0.9818

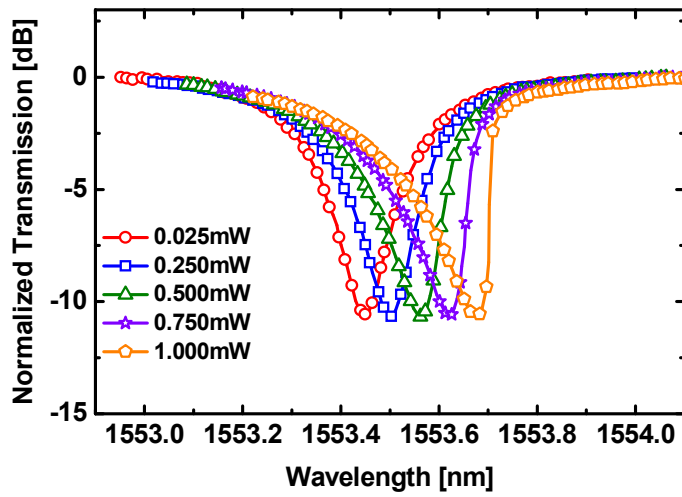


Fig. 3-5. Transmission characteristics of Si MRM with five different input optical powers.

## 3.2. Parametric Characterization of Self-Heating

### 3.2.1. Resonance Wavelength Shift

As the input optical power becomes larger in the depletion-type Si MRM, the resonance wavelength shifts to longer wavelength and the transmission spectrum becomes asymmetric due to self-heating as shown in Fig. 3-5. Fig. 3-6(a) shows the measured resonance wavelength at different input powers for the same device. The red line in Fig. 3-6(b) shows the changes in the effective refractive index of resonance wavelength for different input powers determined from  $m\lambda_{res} = n_{res}L$  which is linearly fitted. The change in the effective index is caused by temperature increase in the ring waveguide by self-heating as well as dispersion of the effective index. Or,

$$\Delta n_{res} = \frac{\delta n_{res}}{\delta T} \Delta T + \frac{\delta n_{res}}{\delta \lambda} \Delta \lambda_{res}. \quad (3.1)$$

With the knowledge of group index as well as the relationship between variation of resonance wavelength and effective refractive index represented as

$$n_g = n_{res} - \lambda \frac{\delta n_{res}}{\delta \lambda}, \text{ and} \quad (3.2)$$

$$\Delta \lambda_{res} = \lambda_{res} \frac{\Delta n_{res}}{n_{res}}, \quad (3.3)$$

the amount of resonance wavelength shift due to only self-heating can

be expressed as [20], [30]

$$\Delta\lambda_{res} = \lambda_{res} \frac{\Delta n_{res}}{n_{res}} = \frac{\lambda_{res}}{n_g} \frac{\delta n_{res}}{\delta T} \Delta T. \quad (3.4)$$

Since it is more convenient to express  $\Delta\lambda_{res}$  as a function of input optical power which can be easily derived from the measurement we can rewrite Eq. (3.4) as

$$\Delta\lambda_{res} = \frac{\lambda_{res}}{n_g} R \Delta I_{in}, \quad (3.5)$$

where  $\Delta I_{in}$  is the input optical power change and  $R$  is a newly-introduced self-heating coefficient. By comparing Eq. (3.4) and Eq. (3.5), we have

$$R = \frac{\delta n_{res}}{\delta T} \frac{\Delta T}{\Delta I_{in}}, \quad (3.6)$$

where  $R$  represents the change in  $n_{res}$  due to temperature change caused by input power increase. As can be seen in Eq. (3.5),  $R$  can be easily determined by measuring the change in resonance wavelength caused by the input power change with the knowledge of the group index. For the Si MRM device measured for Fig. 3-6(a),  $R= 5.67 \times 10^{-4}$  (/mW) can be determined using 3.84 for  $n_g$ . Since the resonance wavelength change is linear for the input power ranges of interest, measurements at two different input power levels should be sufficient for  $R$  determination. With the knowledge of self-heating coefficient  $R$ , we can plot the green line in Fig. 3-6 (b), which represents the effective

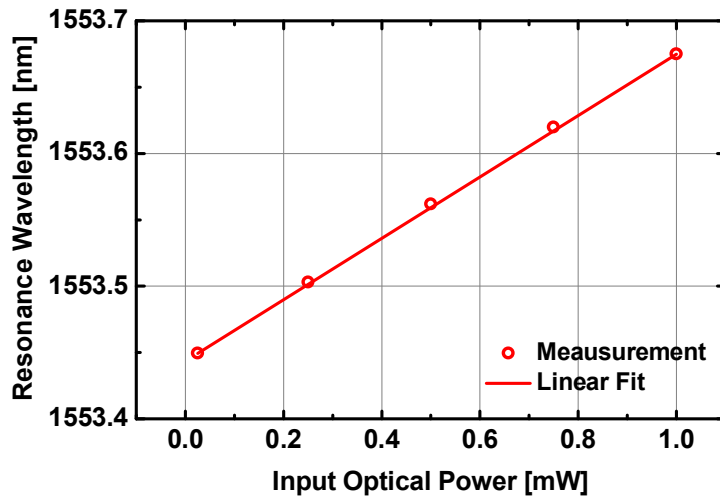
index change due to only temperature change. The difference between green and red lines in Fig. 3-6(b) is the effective index change due to dispersion, which is shown with a blue line in Fig. 3-6(b). Since the sign of dispersion for Si is negative, or Si refractive index decreases with wavelength increase [31], the influence of self-heating is somewhat reduced due to dispersion in Si MRMs.

The optical Kerr effect can also cause linear increase in the refractive index in Si with increasing optical power. However, since the measured index variation is much larger than the possible amount of optical Kerr effect, we can easily determine that this wavelength shift is due to free-carrier absorption. With Kerr coefficient of  $n_2 = 3\sim 6 \times 10^{-18}$  ( $\text{m}^2/\text{W}$ ) for Si [32], [33], the amount of refractive index change due to the Kerr effect in the Si waveguide in our MRM can be estimated much less than those observed in the present investigation. We can also estimate the actual temperature increase in the ring waveguide due to self-heating by approximating  $\delta n_{eff}/\delta T$  with

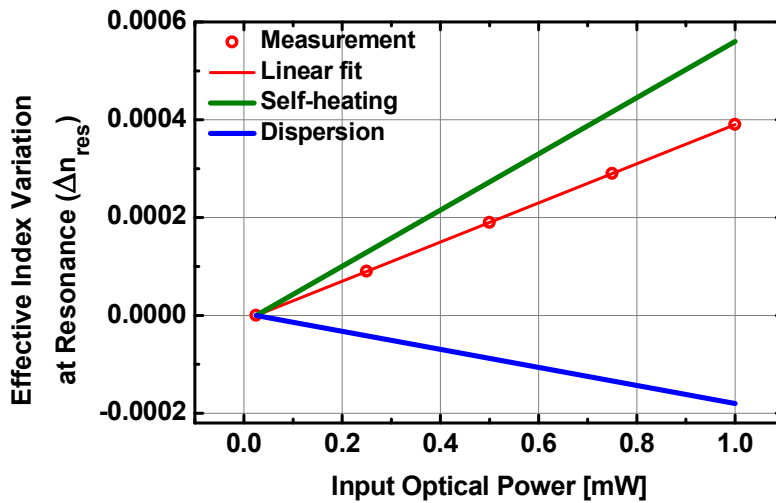
$$\frac{\delta n_{eff}}{\delta T} = \Gamma_{core} \frac{\delta n_{core}}{\delta T} + (1 - \Gamma_{core}) \frac{\delta n_{cladding}}{\delta T}. \quad (3.7)$$

Silicon has thermo-optical coefficient ( $\delta n_{core}/\delta T$ ) of  $1.86 \times 10^{-4}/\text{K}$  [34] and  $\Gamma_{core}$  can be determined to be about 0.72 from numerical simulation, Lumerical FDTD Solution, of the ring waveguide.  $\delta n_{cladding}/\delta T$  can be approximated with thermo-optic coefficient of  $\text{SiO}_2$ , which is about

$1 \times 10^{-5}/\text{K}$  [34], [35]. Since  $\Delta n_{\text{eff}}$  can be determined as  $5.67 \times 10^{-4}/(\text{mW})$  due to self-heating from Fig. 3-6(b), there is about 4.1 degree temperature increase in the ring waveguide.



(a)



(b)

Fig. 3-6. (a) Measured resonance wavelength and (b) effective index variation at resonance wavelength for 5 different input optical powers. In addition estimated effective index variation due to only temperature change and dispersion are shown in (b).

### 3.2.2. Asymmetric Shape of Transfer Curve

The influence of self-heating on the transmission spectrum is recursive in that self-heating changes the resonance wavelength, which in turn changes the amount of self-heating at a given wavelength [36] which makes it had to decide the exact transmission characteristics including self-heating. However, since the amount of red shift due to self-heating should be proportional to the optical power circulating in the ring waveguide for any wavelength near the resonance, we can determine the amount of red shift for any wavelength by the following linear approximation,

$$\Delta\lambda_\lambda \sim \Delta\lambda_{res} \frac{|A_\lambda|^2}{|A_{res}|^2}, \quad (3.8)$$

where  $|A_\lambda|^2$  represents the optical power inside the ring waveguide at near resonance. Fig. 3-7 shows clear definition for  $\Delta\lambda_\lambda$  and  $\Delta\lambda_{res}$ . From the analysis based on the coupled-mode equation,  $|A_\lambda|^2$  can be expressed as [26], [36]

$$|A_\lambda|^2 = |a_\lambda|^2 \frac{c}{nL}. \quad (3.9)$$

Assuming the value of  $n$  in Eq. (3.9) as a fixed value for the wavelength range of interest at a given input power, substituting Eq. (3.9) into Eq. (3.8), and with the knowledge for Eq. (2.12) for  $|a_\lambda|^2$ , we

have

$$\Delta\lambda_\lambda \sim \Delta\lambda_{res} \frac{|a_\lambda|^2}{|a_{res}|^2} = \Delta\lambda_{res} \frac{(2 - \alpha^2 - \gamma^2)^2 c^2}{4n_{res}^2 L^2 (\omega - \omega_r)^2 + (2 - \alpha^2 - \gamma^2)^2 c^2}, \quad (3.10)$$

where all the parameters in the equation except  $\Delta\lambda_{res}$  are MRM parameters determined at low input power without self-heating. In other words, if we measure the MRM transmission spectrum at low input power and the amount of resonance wavelength red-shift due to larger input power, we can determine transmission spectrum at that larger input power using Eq. (3.10).

Fig. 3-8(a) shows measured transmission spectra, same as shown in Fig. 3-5, and calculated spectra using Eq. (3.10) with exacted parameters given in Table 3-1 and measured  $\Delta\lambda_{res}$ . As can be seen, they agree very well, confirming the accuracy of our model. At higher input optical powers, the transmission spectra show bi-stability, which is not consider for the present investigation as bi-stability is not desirable for applications we are interested in.

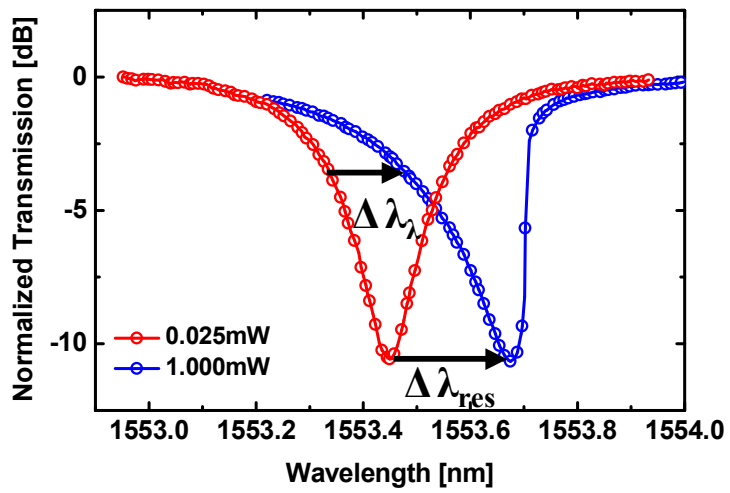
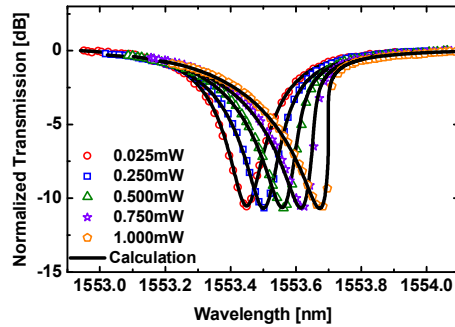
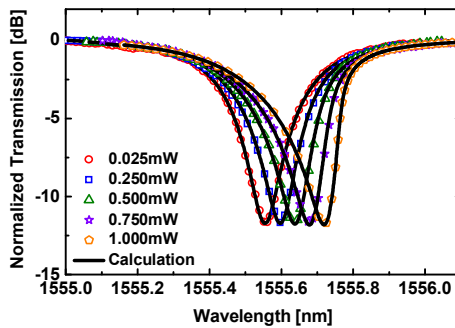


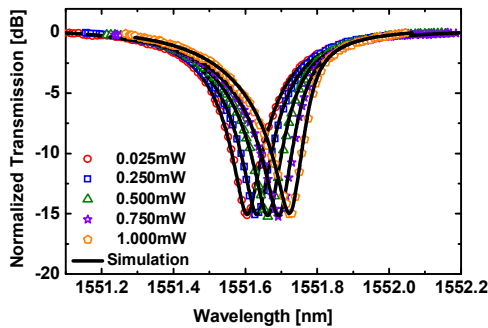
Fig. 3-7. Measured transmission spectra at two different input powers. Asymmetric shape is shown for high input optical power.



(a)



(b)



(c)

Fig. 3-8. Measured and calculated transmission spectra at different input optical powers for Si MRMs having different radii and directional coupler gap distances, (a)  $8\mu\text{m}$  and  $290\text{nm}$ , (b)  $12\mu\text{m}$  and  $250\text{ nm}$ , and (c)  $16\mu\text{m}$  and  $220\text{ nm}$ .

TABLE 3-2  
EXTRACTED SI MRMS PARAMETERS HAVING DIFFERENT RADII

<b>Radius (<math>\mu\text{m}</math>)</b>	8	12	16
<b>Gap (nm)</b>	290	250	220
<b><math>\alpha</math></b>	0.9669	0.9507	0.9323
<b><math>\gamma</math></b>	0.9818	0.9708	0.9523
<b>R (/mW)</b>	5.67E-4	3.99E-4	2.96E-4
<b>R ratio</b>	1.00	0.7	0.52
<b><math> A_{\text{res}} ^2</math> ratio</b>	1.00	0.69	0.52

### 3.2.3. Dependence of Self-Heating Coefficient ( $R$ )

Fig. 3-8 (a), (b), (c) show measured and calculated transmission spectra at different input power levels for three different Si MRM devices having different ring radii and gap distances between ring and bus waveguides. These devices have the same Si MRM structures except ring radius and gap distance. Table 3-2 shows the extracted parameters along with  $R$  and  $|A_{res}|^2$  ratios normalized to the values for 8 $\mu$ m device. As can be shown in the table,  $R$  values differ for different devices. This difference can be explained by noting  $\Delta T/\Delta I_{in}$  in Eq. (3.6) where it can be further expanded as

$$\frac{\Delta T}{\Delta I_{in}} = \frac{\Delta T}{\Delta |A_{res}|^2} \cdot \frac{\Delta |A_{res}|^2}{\Delta I_{in}}. \quad (3.11)$$

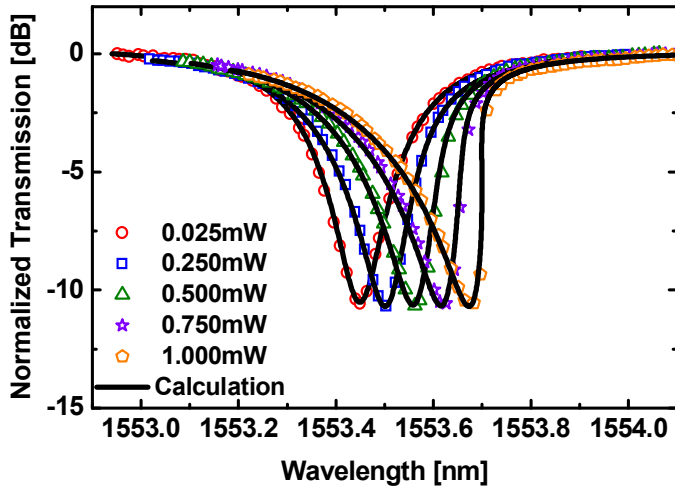
Consequently, Si MRMs can have different  $R$  values due to the difference in  $|A_{res}|^2$  caused by differences in  $\alpha$  and  $\gamma$ . From Eq. (2.12) and Eq. (3.9), we can derive

$$|A_{res}|^2 = \frac{4(1-\gamma^2)}{(2-\alpha^2-\gamma^2)^2} \cdot I_{in}, \quad (3.12)$$

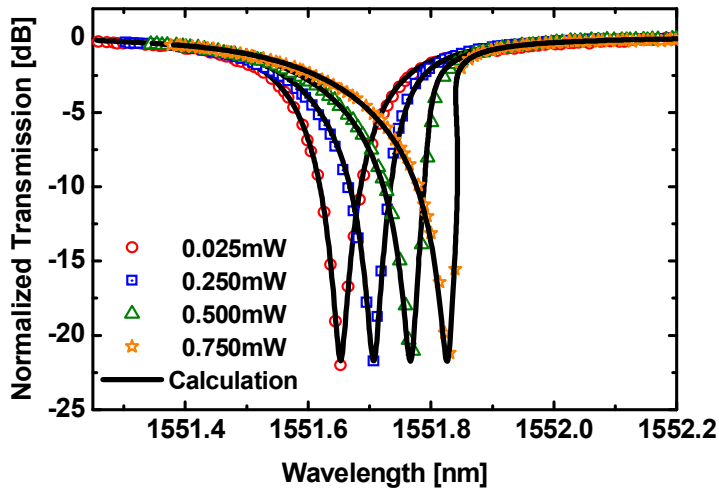
which can be easily calculated using extracted model parameters. The calculated ratios for the optical powers in the ring waveguide at the resonance wavelength are shown in Table 3-2. As can be seen, their ratios are almost identical to  $R$  ratios, indicating the difference in  $R$

values for these three Si MRMs are purely due to the different amount of the optical power inside the ring waveguide at the resonance.

Fig. 3-9 (a), (b) show the measured and calculated transmission spectra at different input power levels for two Si MRM devices having different doping concentrations. Note that Fig. 3-9 (a) is identical to Fig. 3-8 (a), two Si MRM devices differ only their doping concentrations. Table 3-3 shows the extracted parameters along with  $R$  and  $|A_{res}|^2$  ratios normalized to the values for 8um device. Even though the device with lower doping concentration has higher optical power inside the ring, both devices have similar  $R$  values. This is due to the doping concentration dependence of FCA [24], [37], which is related to  $\Delta T/\Delta|A_{res}|^2$  in Eq. (3.11). This clearly shows that doping concentrations as well as device structures influence the amount of optical powers in the ring at the resonance. Consequently, these factors should be carefully considered in order to have clear understanding of self-heating.



(a)



(b)

Fig. 3-9. Measured and calculated transmission spectra at different input optical powers for Si MRMs having different doping concentration, (a)  $7 \times 10^{17} \text{ (cm}^{-3}\text{)}$ ,  $5 \times 10^{18} \text{ (cm}^{-3}\text{)}$  for P-, N-type, (b)  $5 \times 10^{17} \text{ (cm}^{-3}\text{)}$ ,  $3 \times 10^{18} \text{ (cm}^{-3}\text{)}$  for P-, N-type. For (b), 1mW was not included where Si MRM shows bi-stability

TABLE 3-3  
EXTRACTED PARAMETERS FOR SI MRMS HAVING DIFFERENT DOPING  
CONCENTRATION

<b>P/N Doping Concentration</b>	P: $7 \times 10^{17}(\text{cm}^{-3})$ N: $5 \times 10^{18}(\text{cm}^{-3})$	P: $5 \times 10^{17}(\text{cm}^{-3})$ N: $3 \times 10^{18}(\text{cm}^{-3})$
<b><math>\alpha</math></b>	0.9669	0.9801
<b><math>\gamma</math></b>	0.9818	0.9831
<b>R (/mW)</b>	5.67E-4	5.89E-4
<b>R ratio</b>	1.00	1.04
<b><math> A_{\text{res}} ^2</math> ratio</b>	1.00	1.79

## 4. Dynamic Model of Depletion-Type Si MRM

Until now we have focused on steady-state characteristics of Si MRM, from now on we will talk about dynamic modulation of Si MRM and how self-heating influences its dynamics. There are several reports regarding Si MRM modulation characteristics based on either the time-dependent model [38] or coupled-mode theory [39, 40]. The time-dependent dynamics model provides very accurate results but it can be computationally intensive and its use may not be very convenient for the design optimization process. In contrast, the model based on the couple-mode theory is simpler and computationally less intensive. The numerical solution of Si MRM has been widely known and it was implemented in Verilog-A, a popular behavior-level simulator among circuit designers, which can allow simultaneous simulation of Si MRMs and driver electronics [29]. However, even though these numerical approaches can produce accurate results, these approaches have several disadvantages for designing Si MRM such as time consuming. On the other hands, small-signal approximation can be much easier to use for Si MRM design. There are several small-signal model approximations based on coupled-mode approach [41-44]. Their models, based on two-poles one zero system, provide clear

understanding of the frequency response of Si MRM and straightforward systematic explanations of Si MRM modulation for both cases of Si MRM refractive index and coupling coefficient modulation. However, this coupled-mode theory based small-signal model does not give clear understanding how Si MRM dynamic characteristics change with key device parameters. In addition, since it is based on optical parameters, it has limitation on co-simulation with other electrical devices such as modulator driver or thermal controller. In this respect, if such a model can be implemented with an equivalent circuit, knowledge from the well-established circuit theory can be easily utilized for intuitive understanding of Si MRM modulation dynamics. In addition, such a model should be of great use for designing the optimal Si photonic transmitters that include both Si MRMs and driver electronic circuits. Therefore, in this chapter, based on reported coupled-mode based small-signal model, we will focus on its equivalent circuit model of Si MRM. Furthermore, by based on our equivalent circuit model, we also consider Si MRM's voltage dependence to model for large signal input condition. The voltage dependent equivalent circuit parameters are modeled by Verilog-A. And simulated large-signal eye-diagram of a Si MRM is compared with the measurement result.

## 4.1. Small Signal Model

### 4.1.1. Coupled-Mode Approach

Input light in the bus waveguide is partially coupled into the ring waveguide and experiences phase shifts as it circulates in the ring waveguide. In turn, some portion of the circulating light in ring waveguide couples back into the bus waveguide experiencing interference. The amount of output optical power changes with the variation of the ring waveguide effective index, which changes the resonance wavelength of the MRM. The ring waveguide effective index can be electrically modulated with an embedded reverse biased PN junction for high-speed operation [24]. When the Si MRM is modulated with a small-signal junction voltage given as  $V_j(t)=v_0\cos(\omega_m t)$  around the bias voltage, the change in the effective index with time,  $\eta(t)$ , can be expressed as

$$\eta(t) = \frac{\partial \eta}{\partial V_j} v_0 \cos(\omega_m t). \quad (4.1)$$

Considering only the linear response, the output optical signal is also modulated with the same angular frequency  $\omega_m$ . The modulated optical signal is detected by a photodetector, generating photocurrents that are proportional to output optical power,  $P_{out}$ , of the Si MRM. This

process can be modeled in the s-domain based on the coupled-mode equation as [41], [42]

$$\Delta_o(s) = \frac{P_{out}/P_{in}(s)}{V_j(s)} = \frac{4}{\eta_{res}} \cdot \frac{\partial \eta}{\partial V_j} \cdot \frac{\omega_r D / \tau_e}{D^2 + 1/\tau^2} \cdot \frac{s + 2/\tau_l}{s^2 + (2/\tau)s + D^2 + 1/\tau^2}, \quad (4.2)$$

where  $P_{in}$  is the input optical power,  $D (= \omega_{in} - \omega_r)$ , detuning parameter, represents how much the input light angular frequency  $\omega$  is detuned from the ring resonance angular frequency  $\omega_r$ , and  $\eta_{res}$  represents the effective refractive index of the ring waveguide at the given bias voltage.  $\tau_l$  and  $\tau_e$  are decay time constants of the ring resonator due to the round-trip loss and ring-bus coupling, respectively. They satisfy  $1/\tau_l + 1/\tau_e = 1/\tau$ , where  $\tau$  is the total decay time constant for the ring resonator. Eq. (4-2) represents a two-pole and one-zero linear system whose damping factor  $\zeta$  and natural frequency  $\omega_n$  are given as

$$\zeta = \frac{1}{\sqrt{1 + D^2 \tau^2}}, \quad \text{and} \quad (4.3)$$

$$\omega_n = \sqrt{D^2 + \frac{1}{\tau^2}}. \quad (4.4)$$

Since  $\zeta$  is smaller than 1 unless  $D=0$ , the Si MRM has the underdamped modulation frequency response except at the resonance frequency. Based on this coupled-mode based small-signal model, equivalent circuit model of Si MRM can be derived.

### 4.1.2. Equivalent Circuit Model

With the knowledge of optical modulation characteristics of Si MRM mentioned in previous chapter, we can model equivalent circuit of Si MRM by considering with its electrical characteristics. To be specific, the linear frequency modulation characteristics of a Si MRM can be modeled in three steps as shown in Fig. 4-1 having three blocks: parasitic components for pads and interconnects ( $B_{\text{Para}}$ ), electrical components for Si MRM core ( $B_{\text{Core}}$ ), and a lossy LC tank ( $B_{\text{Opt}}$ ) that represents small-signal optical modulation characteristics of Si MRM. Detailed explanations for each block are given below.

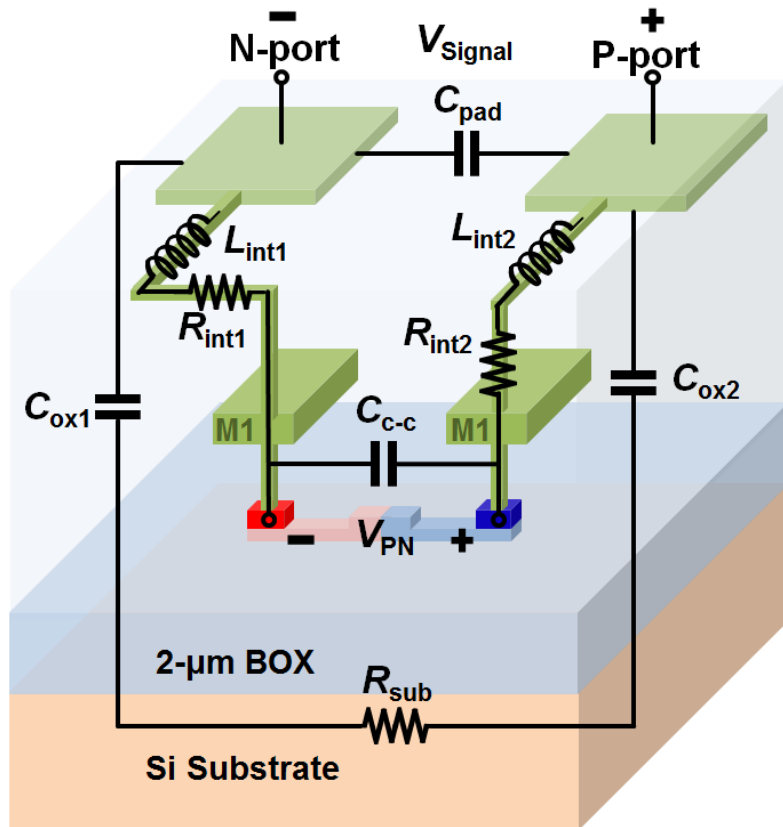


Fig. 4-1. Block diagram of equivalent circuit for Si MRM.

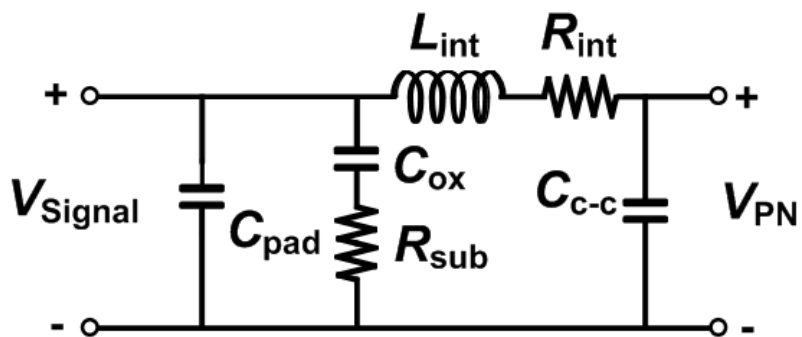
### 4.1.2.1. Pads and Interconnects ( $B_{\text{Para}}$ )

In previously reported models for Si MRMs, the influence of pads and interconnects has been considered together with the Si MRM core and simply modeled by one capacitor [29], [44], [45]. However, as the required modulation speed increases, the effect of these parasitic components becomes more significant and including an accurate model for them becomes necessary. Fig. 4-2 (a) shows the parasitic components that should be considered.  $C_{\text{pad}}$  is the capacitance between two signal pads as well as metallic interconnects lines,  $C_{\text{ox1}}$ ,  $C_{\text{ox2}}$  are the capacitance between pad and silicon substrate for N-port and P-port, respectively.  $R_{\text{sub}}$  is the resistance through the silicon substrate connected to N-port and P-port pads through  $C_{\text{ox1}}$  and  $C_{\text{ox2}}$ .  $L_{\text{int1}}$ ,  $L_{\text{int2}}$ ,  $R_{\text{int1}}$ , and  $R_{\text{int2}}$  are inductances and resistances of interconnect lines for N-port and P-port terminals.  $C_{\text{c-c}}$  represents the capacitance between two metal openings to N+ and P+ regions. The output voltage of this block is the voltage across the Si MRM PN junction ( $V_{\text{PN}}$ ). With the knowledge that the same amount of current flows in both N-port and P-port interconnect lines for the two-terminal Si MRM, we can simplify the circuit by using  $C_{\text{ox}}=C_{\text{ox1}}||C_{\text{ox2}}$ ,  $L_{\text{int}}=L_{\text{int1}}+L_{\text{int2}}$ , and  $R_{\text{int}}=R_{\text{int1}}+R_{\text{int2}}$ , and simplify  $B_{\text{Para}}$  as shown in Fig. 4-2 (b). Determination of

the numerical value for each component can be done with EM simulation and the open and short test patterns [46] that are fabricated on the same die as the Si MRM device.



(a)

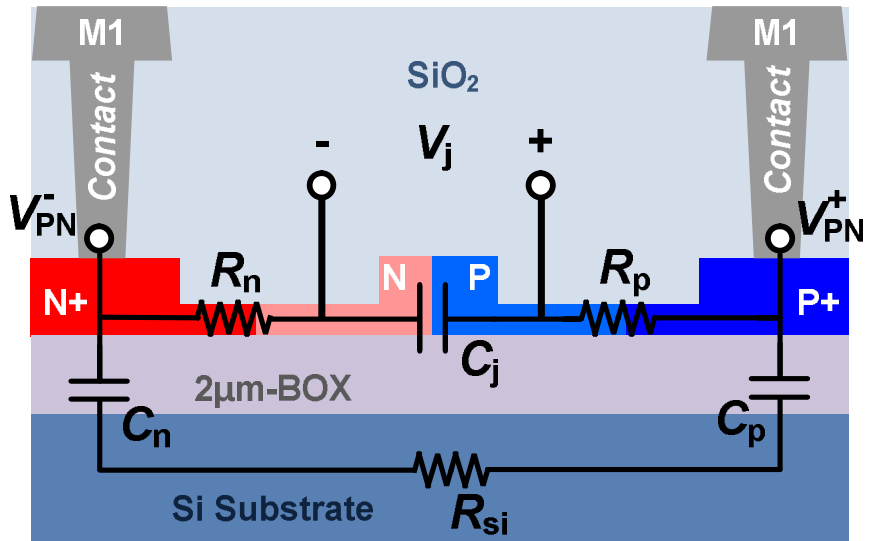


(b)

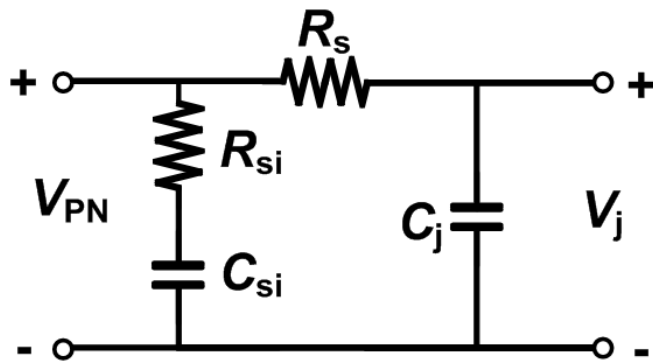
Fig. 4-2. (a) Parasitic components of pads and interconnects, and (b) its equivalent circuit ( $B_{para}$ ).

#### 4.1.2.2. Si MRM Core ( $B_{Core}$ )

As shown in Fig. 4-3 (a), the Si MRM core can be modeled with RC components [29], [44], [45].  $C_j$  represents the junction capacitance for PN-junction,  $R_n$  and  $R_p$  represent the resistances in the doped Si layers,  $C_n$  and  $C_p$  represent the capacitance between doped silicon layers and the silicon substrate, and  $R_{si}$  represents the resistance of the silicon substrate below the Si MRM device. Fig. 4-3 (b) shows the equivalent circuit of the Si MRM core where  $R_s=R_n+R_p$  and  $C_{si}=C_n||C_p$ . The output signal of this block is the voltage across  $C_j$  since light in the Si MRM is modulated by the effective index variation due to the junction voltage ( $V_j$ ) variation. Once we know  $B_{Para}$ , we can determine the numerical value for each component in  $B_{Core}$  by fitting magnitude and phase of simulated S11 into measured values



(a)



(b)

Fig. 4-3. (a) Cross section as well as electrical components for Si MRM core, and (b) its equivalent circuit ( $B_{Core}$ ).

### 4.1.2.3. Optical Characteristics ( $B_{\text{Opt}}$ )

Fig. 4-4 represents the corresponding equivalent circuit model for the small-signal modulation characteristics of the Si MRM given in Eq. (4.2). Here,  $V_{\text{out}}$  represents normalized output power ( $P_{\text{out}}/P_{\text{in}}$ ). Unlike the circuit model given in [43], it is composed of a lossy  $LC$  tank with a voltage-controlled current source having transconductance  $g$  and two additional resistors,  $R_1$  and  $R_2$ . The transfer function in the  $s$ -domain for the equivalent circuit shown in Fig. 4-4 is given as

$$\Delta(s) = \frac{V_{\text{out}}(s)}{V_j(s)} = \frac{g}{C} \frac{s + \frac{R_2}{L}}{s^2 + \left( \frac{1}{CR_1} + \frac{R_2}{L} \right) s + \frac{1}{LC} \left( \frac{R_2}{R_1} + 1 \right)}. \quad (4.5)$$

By comparing Eq. (4.2) and Eq. (4.5), we can determine the relationship between Si MRM device parameters ( $\tau_e$ ,  $\tau_l$ ,  $D$ ) and circuit model parameters ( $R_1$ ,  $R_2$ ,  $L$ ,  $C$ )

$$R_1 C = \frac{\tau_e}{2}, \quad (4.6)$$

$$\frac{L}{R_2} = \frac{\tau_l}{2}, \quad (4.7)$$

$$\frac{R_1}{R_2} = \left[ (1/\tau^2 + D^2) \tau_e \tau_l / 4 - 1 \right], \quad (4.8)$$

$$g = \frac{2P_{\text{in}}}{\eta_0} \cdot \frac{\partial \eta}{\partial v} \cdot \frac{\omega_r D}{D^2 + 1/\tau^2} \frac{1}{R_1} U. \quad (4.9)$$

The unit conversion factor  $U$  ( $= 1\text{V}$ ) is added in Eq. (4.9) so that  $g$  can

have the correct unit of transconductance. Our model preserves the physical meaning of the two time constants of the ring resonator by representing time constant  $\tau_e$  with  $R_1C$  and  $\tau_l$  with  $L/R_2$ . The factor of two shows up in Eq. (4.6) and Eq. (4.7) because  $\tau_e$  and  $\tau_l$  are time constants for electrical fields whereas the equivalent circuit models the optical power. Damping factor  $\zeta$  and natural frequency  $\omega_n$  are given as

$$\zeta = \frac{CR_1R_2 + L}{2\sqrt{LCR_1(R_1 + R_2)}}, \quad (4.10)$$

$$\omega_n = \sqrt{\frac{1}{LC} \left( \frac{R_2}{R_1} + 1 \right)}. \quad (4.11)$$

Since all circuit model parameters are directly related to Si MRM device parameters, their values can be easily determined from transmission characteristics of the Si MRM.

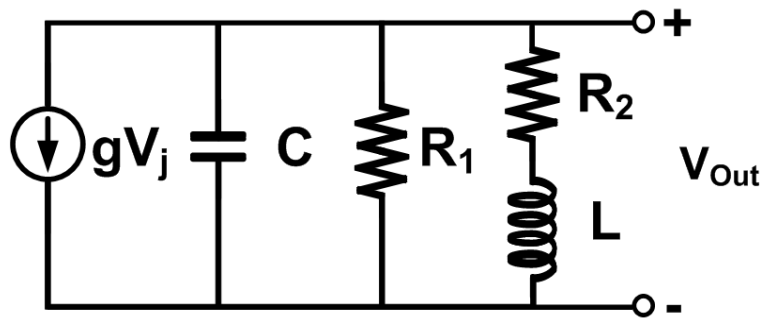


Fig. 4-4. Equivalent circuit of Si MRM optical modulation characteristics ( $B_{Opt}$ ).

#### 4.1.2.4. Measurement and Model Verification

To confirm our equivalent circuit model, we have extracted each parameter from DC measurement and compared frequency response based on our suggested model with measured  $S_{11}$ . The structure of Si MRM is same as Fig. 3-3 where the nominal peak doping concentration of  $7 \times 10^{17} (\text{cm}^{-3})$  for P-region and  $3 \times 10^{18} (\text{cm}^{-3})$  for N-region.  $B_{\text{Para}}$  can be determined from electrical  $S_{11}$  measurement of short and open test patterns having the same pad structures and interconnect lines as the target Si MRM fabricated on the same die [46]. For the short test pattern, the N-port and P-port are shorted in the Metal-1 layer, while they are open for the open test pattern. Since neither short nor open test pattern includes  $C_{\text{c-c}}$ , we first determined the value of  $C_{\text{c-c}}$  by EM simulation. By fitting simulated  $S_{11}$  values to measured values, we can determine the numerical value for each component in  $B_{\text{Para}}$  as shown in Table 4-1. With  $B_{\text{Para}}$  known,  $B_{\text{Core}}$  can be determined by fitting simulated  $S_{11}$  values for our  $B_{\text{Para}}$  &  $B_{\text{Core}}$  model into measured values. Fig. 4-5 shows the magnitude and phase response of measured (circles) and simulated (colored solid line)  $S_{11}$  values with extracted parameter values listed in Table 4-1 at  $V_{\text{signal}} = -1\text{V}$ .

For  $B_{\text{Opt}}$ , values for  $L$ ,  $C$ ,  $R_1$ , and  $R_2$  can be determined from  $\tau_e$  and

$\tau_1$  and  $D$  using equations Eq. (4.6) ~ (4.8), which are extracted from the transmission measurement Si MRM. Fig. 4-6 shows the experimental setup used for this characterization in which a tunable laser and an optical spectrum analyzer are used. With the knowledge of  $R_1$  value,  $g$  can be determined from optical parameters,  $\eta_0$ ,  $D$ ,  $\omega_r$ ,  $\tau$  and  $\delta\eta/\delta v$ . The measured transmission characteristics for a Si MRM biased at -1V are shown in Fig. 4-7. For this measurement, input optical power after grating coupler is minimized to -15 dBm in order to avoid any self-heating. With the knowledge of  $R_1$  value,  $g$  can be determined from optical parameters,  $\eta_0$ ,  $D$ ,  $\omega_r$ ,  $\tau$  and  $\delta\eta/\delta v$ . For determination of  $\eta_0$ , the ring resonance mode number  $m$  can be first identified as 85 from waveguide simulation of the Si MRM. With this,  $\eta_0$  can be determined as 2.63714 at  $V_{\text{signal}} = -1\text{V}$  from the resonance condition  $m\lambda_{\text{res}}=L\eta_0$  with measured  $\lambda_{\text{res}}$ . The value of  $\tau_e$ ,  $\tau_1$ , can be determined by fitting the Si MRM steady-state transmission characteristic, Eq. (2.14), to the measured transmission characteristics as shown in Fig. 4.7 at  $V_{\text{signal}} = -1\text{V}$  with the minimum mean squared error. Extracted values of optical parameters are listed in Table 4-2, and corresponding  $B_{\text{Opt}}$  parameter values at three different detuning values are listed in Table 4-3, where  $R_2$  is fixed at 10K $\Omega$  for convenience.

Fig. 4-8(a) shows the complete equivalent circuit. The simulated

Si MRM modulation frequency responses at three different detuning values are shown in Fig. 4-8(b) along with the measured results. For the measurement, a lightwave component analyzer is used as shown in Fig. 6. The simulation is done with Cadence Spectre (Virtuoso Version No. 14.1.0.459), a popular circuit simulator, using circuit values given in Table 4-1 and Table 4-3. Clearly, different modulation frequency responses of Si MRM at different detuning conditions are accurately modeled with our equivalent circuit

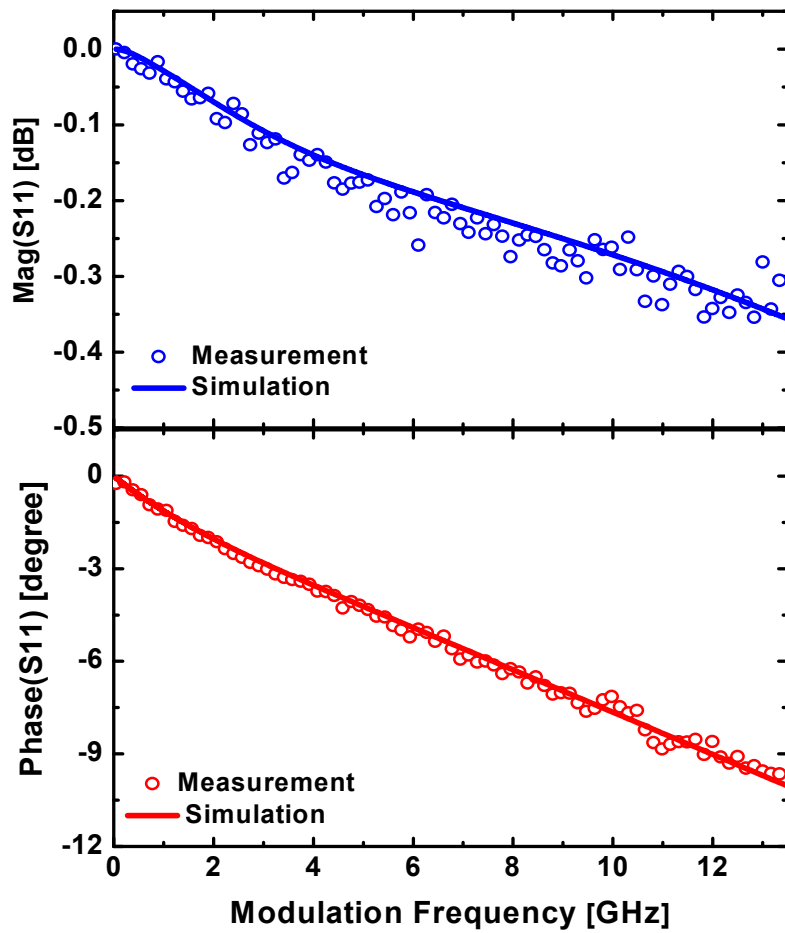


Fig. 4-5. Measured (circles) and simulated (colored solid line)  $S_{11}$  of Si MRM.

TABLE 4-1  
EXTRACTED PARAMETER VALUES FOR  $B_{\text{PARA}}$  AND  $B_{\text{CORE}}$

<b>Parameter</b>	<b>Value</b>
$C_{\text{pad}}$	4.9fF
$C_{\text{OX}}$	5.8fF
$R_{\text{sub}}$	3.9K Ohm
$L_{\text{int}}$	108pH
$R_{\text{int}}$	1.1 Ohm
$C_{\text{c-c}}$	5fF
$R_{\text{si}}$	23K Ohm
$C_{\text{si}}$	7fF
$R_{\text{s}}$	365.5Ohm
$C_{\text{j}}$	8.2fF

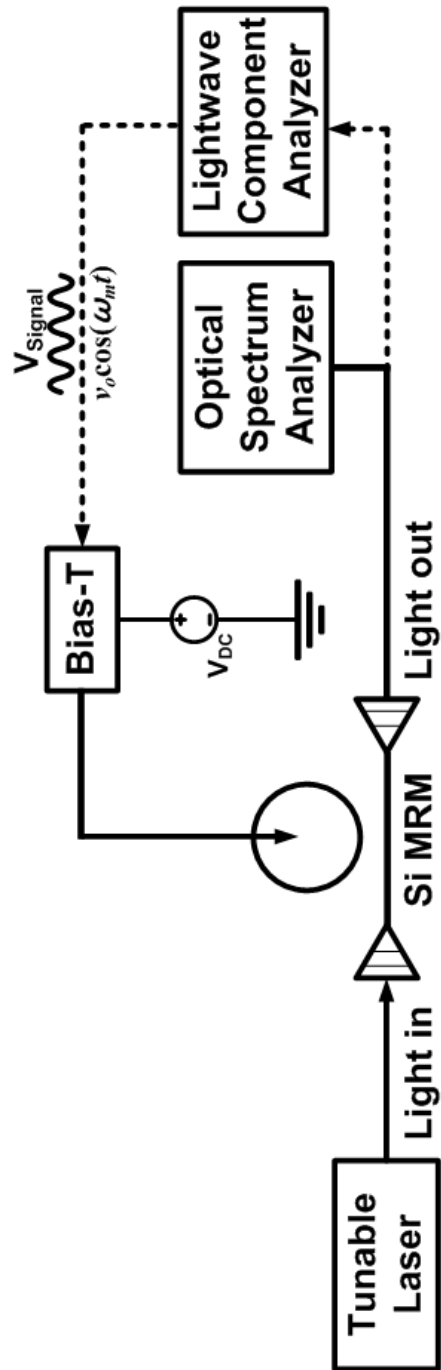


Fig. 4-6. Experimental setup for parameter extraction of  $B_{Opt}$  of Si MRM and frequency response.

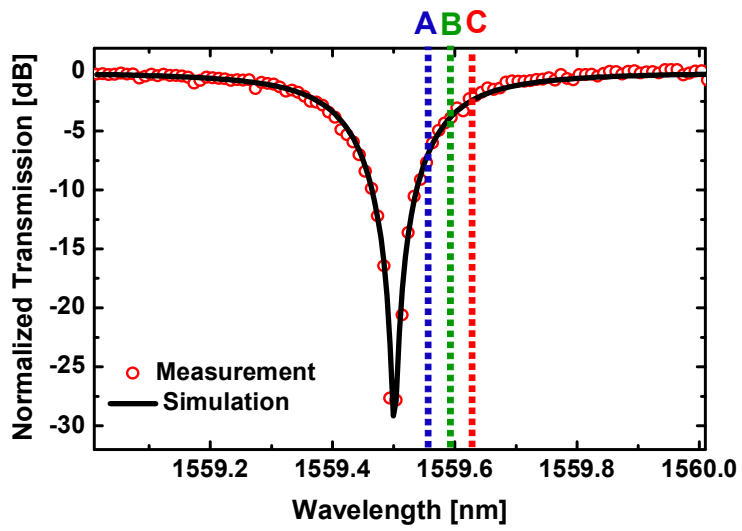


Fig. 4-7. Measured and simulated transmission characteristic of Si MRM.

TABLE 4-2  
EXTRACTED OPTICAL PARAMETER VALUES  
OF SI MRM AT  $V_{\text{SIGNAL}} = -1$

Parameter	Description	Value
$\eta_0$	Effective refractive index of ring waveguide	2.63714
$\tau_e$	Ring-bus coupling decay time constant (ps)	24.635
$\tau_l$	Round-trip loss decay time constant (ps)	22.882

TABLE 4-3

CALCULATED CORRESPONDING  $B_{OPT}$  PARAMETER FROM TABLE 4-2

$D= \omega_{in}-\omega_{res} $ $( \lambda_{in}-\lambda_{res} )$	(A) 50.3RAD/S (65PM)	(B) 73.6RAD/S (95PM)	(C) 96.8RAD/S (125PM)
$R_1$ (K $\Omega$ )	3.6	7.6	13.2
$R_2$ (K $\Omega$ )	10		
$C$ (fF)	3.43	1.61	0.93
$L$ (nH)	114.41		

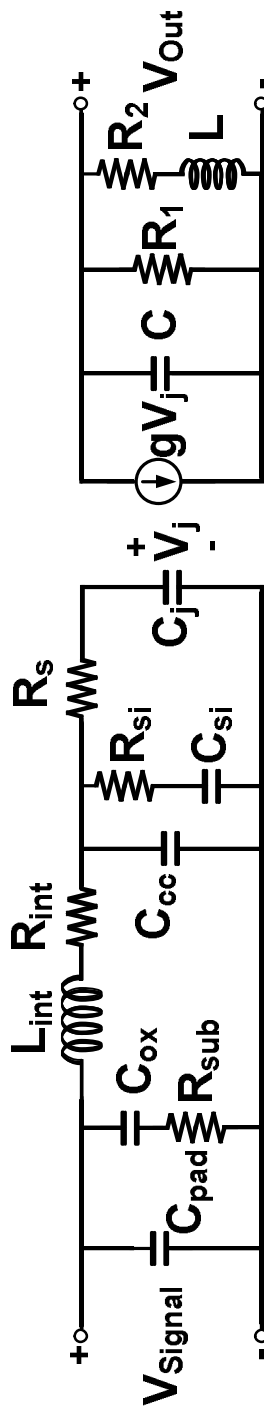


Fig. 4-8. (a) Full equivalent circuit model of Si MRM.

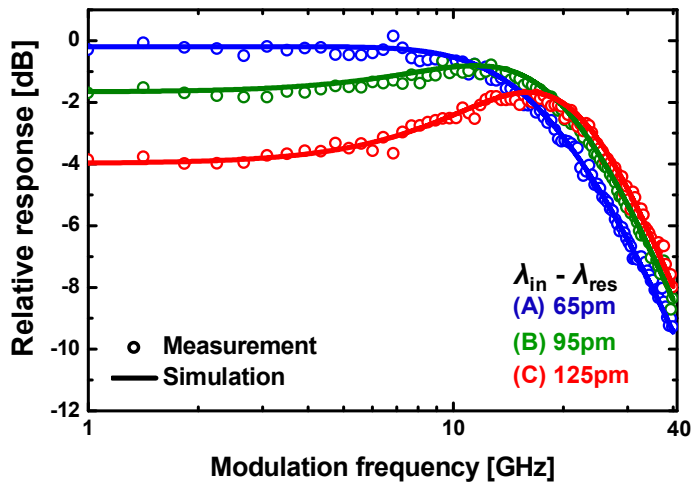


Fig. 4-8. (b) Measured (circles) and simulated (solid line) relative frequency responses at three different detuning levels.

### 4.1.2.5. Application of the Equivalent Circuit

Using our model, we can identify how much each of  $B_{\text{para}}$ ,  $B_{\text{Core}}$  and  $B_{\text{Opt}}$  contributes to the modulation frequency response. Fig. 4-9 shows the simulated normalized modulation frequency responses for only parasitic components ( $B_{\text{Para}}$ ), including parasitic and core components ( $B_{\text{Para}} \& B_{\text{Core}}$ ), and full equivalent circuit model ( $B_{\text{Para}} \& B_{\text{Core}} \& B_{\text{Opt}}$ ) for three different detuning conditions. For the Si MRM device under investigation, the 3-dB modulation bandwidth due to electrical components is approximately 65GHz and, consequently, the modulation frequency response is mainly limited by  $B_{\text{Opt}}$ . It is possible to enlarge the bandwidth of  $B_{\text{Opt}}$  by reducing Q-factor of the ring resonator, or by designing a Si MRM having lower value for  $\tau$  but at the cost of reduced modulation gain as can be seen in Eq. (4.9).

The real advantage for an electrical equivalent circuit for the Si MRM is the ease with which it can be co-simulated with electronic circuits in a similar manner as has been demonstrated for Mach-Zehnder modulators and electro-absorption modulators [47, 48]. Fig. 4-10 (a) shows a schematic for a Si transmitter based on a pseudo differential cascode common-emitter driver and a Si MRM. Such an integrated Si transmitter can be fabricated with IHP's EPIC technology

which provides monolithic integration of 0.25- $\mu\text{m}$  SiGe BiCMOS and Si PIC technologies [49]. In this transmitter, the value of load resistance  $R_L$  should be carefully optimized. Fig. 4-10 (b) shows the simulated gain-bandwidth product as a function of  $D$  as well as  $R_L$  with the simulated frequency responses for selected points is shown in Fig. 4-11 (a) for different  $D$  values and in Fig. 4-11 (b) for different  $R_L$  values. Clearly, the gain-bandwidth product is a sensitive function of electrical characteristics represented by  $R_L$  and optical characteristics represented by  $D$ , and the capability to co-simulate Si MRM in the form of its equivalent circuit along with electronic circuits in the standard electronic circuit simulation environment can be of great advantage for efficient design of Si photonic transmitters based on Si MRMs.

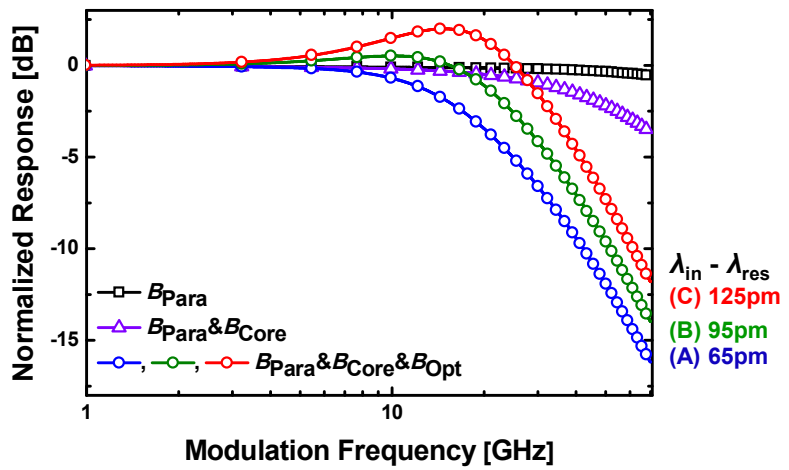
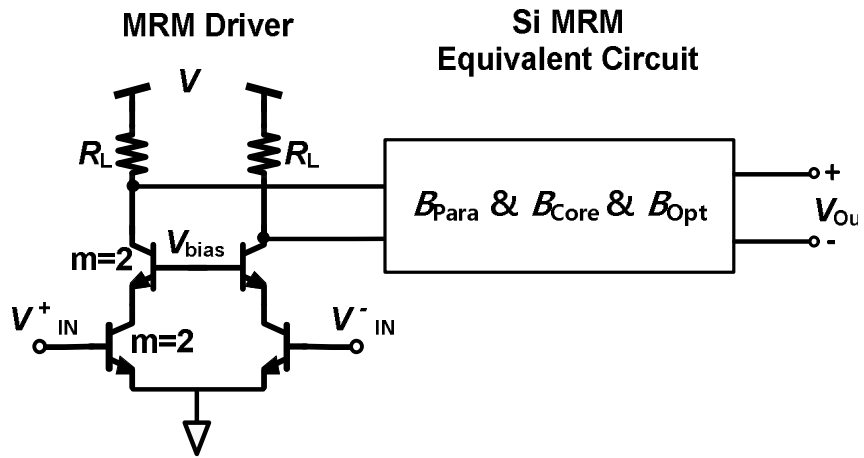
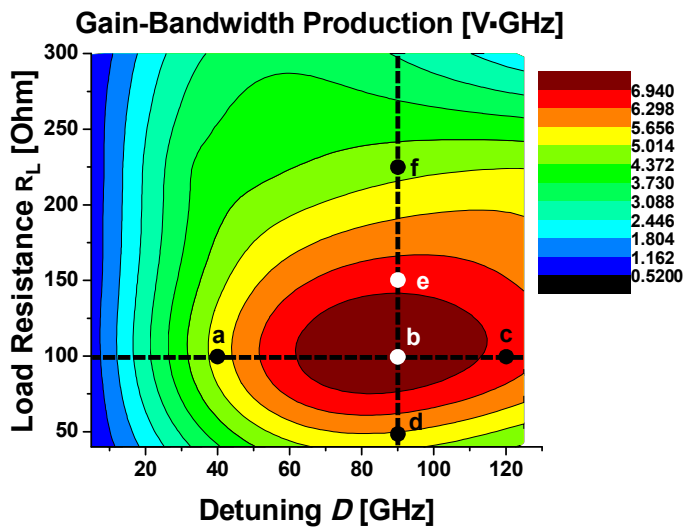


Fig. 4-9. Simulated normalized frequency responses of  $B_{Para}$ ,  $B_{Para} \& B_{Core}$  and  $B_{Para} \& B_{Core} \& B_{Opt}$  at three different detuning levels.

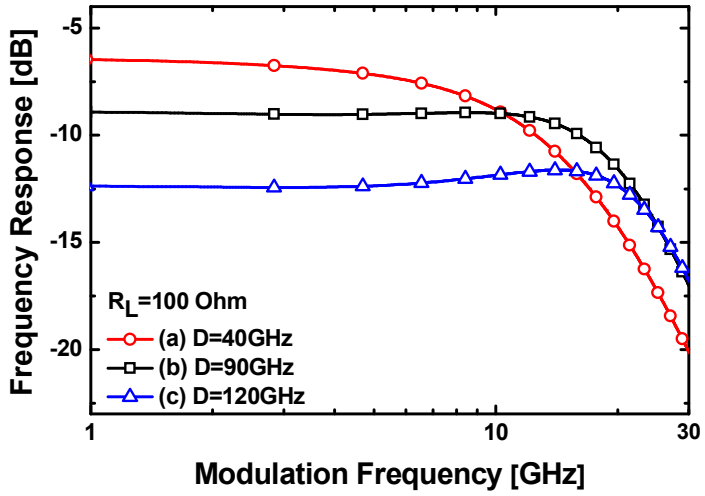


(a)

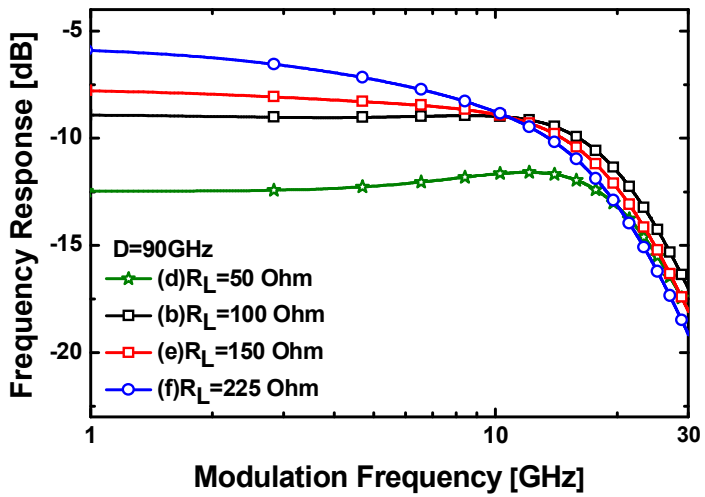


(b)

Fig. 4-10. (a) Schematic of transmitter used for simulation including driver and Si MRM. (b) Simulated gain-bandwidth product of transmitter with different detuning ( $D$ ) as well as driver load impedance ( $R_L$ ).



(a)



(b)

Fig. 4-11. Simulated frequency response of transmitter with (a) three different detuning conditions at  $R_L = 100 \Omega$  and (b) four different  $R_L$  at  $D = 90 \text{ GHz}$

#### **4.1.2.6. Influence of Self-Heating in Small-Signal Model**

Until now, we have studied the small signal model of Si MRM and its equivalent circuit model. From now on, we will talk about how self-heating can affect small-signal model of Si MRM. Since the time scale for self-heating much larger than the modulation time scale of interest, self-heating does not directly affect the modulation frequency responses. This can be easily understand with Fig. 4-12, identical to Fig. 3-7, where blue-dot has same frequency response with red dot where normalized transmission output power is same. To be specific, in the view of steady-state condition, with the high input optical power, the blue-dot has shifted from the red-dot. However, in the view of dynamic condition, since the time constant of self-heating is much slower than the modulation frequency, it does not affect its frequency response and the frequency response of blue-dot is same with the frequency response of red-dot. Therefore, frequency response for high input optical power condition can be substituted by corresponding low input optical power frequency response where self-heating is negligible. Therefore, corresponding low input optical power frequency response can be estimated with self-heating coefficient ( $R$ ). To be specific, shown in Fig.

4-12, since we can estimate  $\Delta\lambda_1$ , from Eq. (3.8), we can calculate the detuning with different input optical power as

$$D(I_{in}) = 2\pi c \left( \frac{|A_{res}|^2}{|A_{res}|^2 \lambda_{in} - |A_1|^2 \frac{\lambda_{res}}{n_g} R I_{in}} - \frac{1}{\lambda_{res}} \right), \quad (4.12)$$

where  $\lambda_{in}$  represents the input optical wavelength. This can be confirmed with Fig. 4-13 which shows 3 different frequency responses for two different input optical powers. Fig. 4-13 (a) shows the transmission characteristics for two different optical power, 0.025mW and 0.500mW. The input wavelengths which have same symbols have same normalized transmission output value noticing that symbol of higher input optical power is shifted by self-heating. As shown in Fig. 4-13 (b), (c), for same normalized transmission output value, regardless of input optical powers, the frequency response is same each other. Furthermore, shown in Fig. 4-13 (b), based on Eq. (4.2) and (4.12), we have simulated the small-signal response for different wavelength as well as input optical powers which were well-matched with measurement result. This convince the accuracy of our model

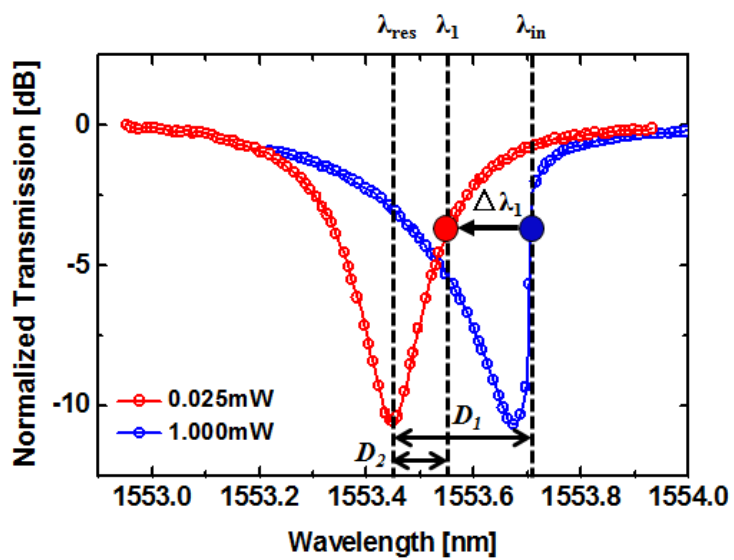
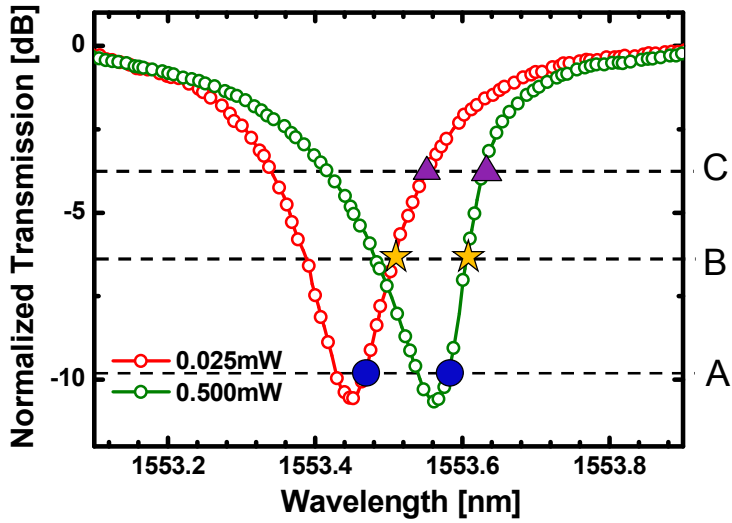
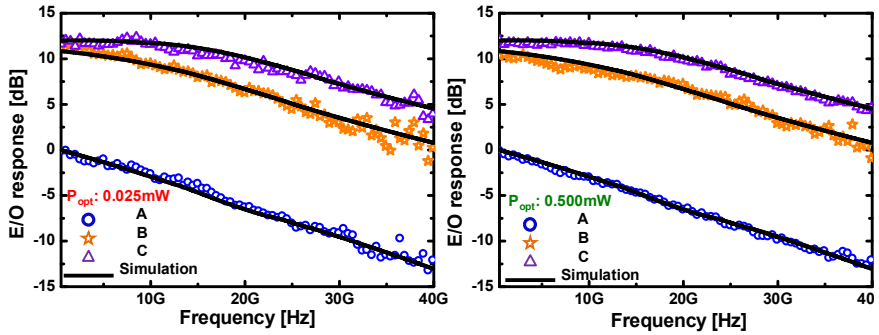


Fig. 4-12 Influence of self-heating in modulation dynamics. Blue dot (1.000mW) has same modulation dynamics with red dot (0.025mW).



(a)



(b)

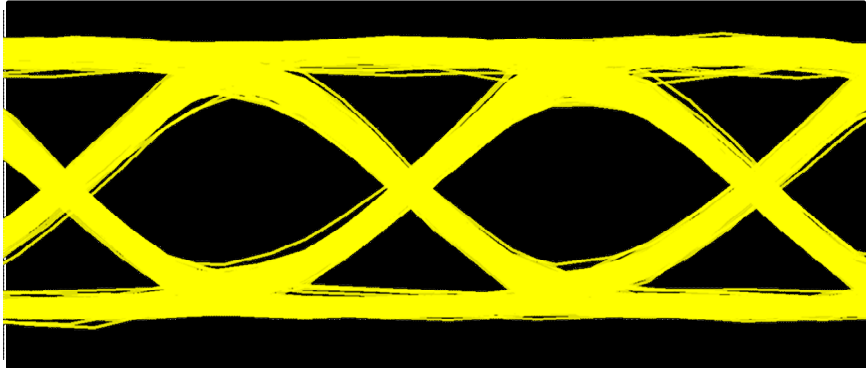
Fig. 4-13. Transmission characteristics for two different optical power, 0.025mW and 0.500mW where same symbols have same normalized transmission output value. (b) Normalized frequency responses for two different input optical powers. Input optical wavelengths are notified in (a).

## 4.2. Large- Signal Model

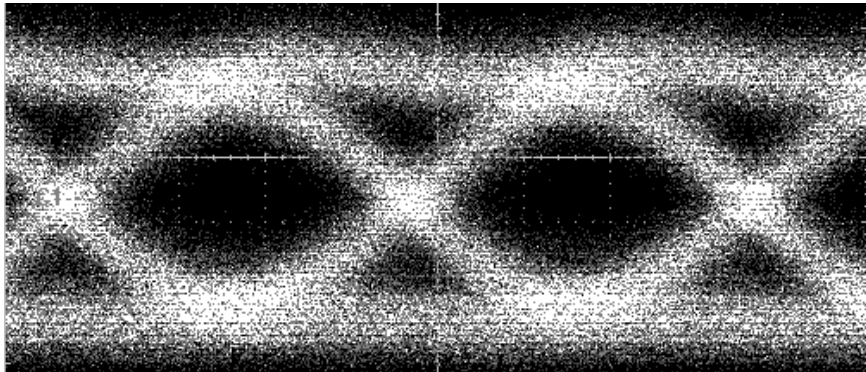
Large-signal simulation is also possible with our model. Since the PN junction capacitance ( $C_j$ ) and round-trip loss ( $\tau_l$ ) nonlinearly depends on the bias voltage,  $C_j$  and  $C$  should be modeled with a voltage-controlled capacitor and also  $R_1$  and  $R_2$  with a voltage-controlled resistor. Such voltage-controlled circuit elements can be easily handled with Verilog-A and imported into Cadence Spectre once parameter values at different bias voltages are known. Fig. 4-14(a) shows a simulated large-signal eye-diagram for the Si MRM modulated with 25-Gb/s PRBS 231-1, 2 Vp-p input obtained with the simulation of our model using parameters values given in Table 4-1 and Table 4-4. When determining  $g$  for different voltages from Eq. (4-9), each  $D$  is calculated independently for different bias voltages with different resonance wavelength. For  $\delta\eta/\delta v$ , we used average value of effective refractive index variation from 0V to -2V. For this simulation, input optical wavelength is 60pm separated from the resonance wavelength at  $V_{\text{signal}}=0\text{V}$ . The value for  $L$  for the inductor in the lossy LC tank is fixed for the reference same as in Table 4-3. Fig. 4-14(b) shows the measured eye diagram and, as can be seen, simulated and measured results agrees well.

TABLE 4-4  
 CALCULATED CORRESPONDING  $B_{OPT}$  PARAMETER  
 FOR DIFFERENT  $V_{BIAS}$  AT  $\Lambda_{IN}=1559.546\text{NM}$

$V_{Bias}$	0V	1V	2V
$C_j$ (fF)	12.0	8.2	6.5
$g$ ( $1/\Omega$ )	$3.2 \times 10^{-5}$	$4.9 \times 10^{-5}$	$6.8 \times 10^{-5}$
$R_1$ (K $\Omega$ )	3.1	1.7	10.2
$R_2$ (K $\Omega$ )	10.2	10	9.9
$C$ (fF)	4.02	7.14	12.12
$L$ (nH)	114.41		



(a)



(b)

Fig. 4-14. (a) Simulated and (b) measured eye diagrams for 25-Gb/s PRBS 231-1 pattern at the input wavelength of 1559.546nm

## 5. Conclusion

We investigated the influence of self-heating on the transmission spectrum and the modulation dynamics of the depletion-type Si MRM. FCA in the doped ring waveguide causes temperature rise and increases the effective index, which changes the resonance wavelength and the transmission spectrum. We introduced the self-heating coefficient ( $R$ ), which can be easily measured and with which changes of the effective index at the resonance wavelength due to self-heating can be precisely modeled. Although it takes transmission spectrum measurements at two different optical input power levels for determining  $R$ , transmission spectra as well as the exact value of Si MRM resonance wavelength shift can be determined at any input power level with the knowledge of  $R$  as demonstrated in our paper. The accuracy of our self-heating model was confirmed by comparing measured transmission spectra for several different Si MRM devices with calculated spectra based on our model. In addition, we clarified the influence of device size and doping concentration on  $R$ .

Furthermore, equivalent circuit model of Si MRM including three blocks is presented: parasitic components, core Si MRM PN junction, and the small-signal modulation characteristics of the Si MRM. The

circuit model parameters are extracted from relatively simple device measurement and simulation. In addition, it has expanded to large-signal model by considering voltage dependent parameters such as,  $C_j$ ,  $g$ ,  $C$ ,  $R_1$ ,  $R_2$ . The accuracy of our models is confirmed with measurement results. Our circuit model allows efficient co-simulation of Si MRMs with electronic circuits in the standard electronic circuit simulation environment. As a result, both parametric characterization of self-heating and equivalent circuit model should provide useful guidelines for designing and analyzing Si MRM that suffer less from self-heating and also for design optimization of electronic-photonic ICs that include Si MRMs.

## Bibliography

[1] N. Savage, "Linking with light [high-speed optical interconnects]," *IEEE Spectrum*, 39 (8), pp. 32-36, Aug. 2002.

[2] <http://www.intel.com/content/dam/www/public/us/en/documents/technology-briefs/intel-labs-hybrid-silicon-laser-announcement.pdf>, M Paniccia, "First electrically pumped hybrid silicon laser.ppt," Oct 2006.

[3] D. Liang, G. Roelkens, R. Baets, and J. E. Bowers, "Hybrid Integrated Platforms for Silicon Photonics," *Materials*, 3(3), pp. 1782-1802, Mar. 2010.

[4] R. Soref, "The past, present, and future of silicon photonics," *IEEE J. Sel. Top. Quantum Electron.*, vol. 12, no. 6, pp. 1678-1687, 2006.

[5] Q. Xu, B. Schmidt, S. Pradhan, and M. Lipson, "Micrometre-scale silicon electro-optic modulator," *Nature* vol. 435, pp. 325-327, 2005

[6] J. F. Buckwalter *et al.*, "A Monolithic 25-Gb/s Transceiver With Photonic Ring Modulators and Ge Detectors in a 130-nm CMOS SOI Process," *IEEE Journal of Solid-State Circuits*, vol. 47, no. 6, pp. 1309-1322, June 2012.

[7] L. Zimmermann, D. J. Thomson, B. Goll, D. Knoll, S. Lischke, F. Y. Grades, Y. Hu, G. T. Reed, H. Zimmermann, H. Porte, "Monolithically integrated 10Gbit/sec Silicon modulator with driver in 0.25 $\mu$ m SiGe:C BiCMOS," European Conference on Optical Communication (ECOC)(2013).

- [8] <http://web.eecs.ytk.edu/~dongarra/ccgsc2006/Slides/>, “Talk2: David Scott.ppt”.
- [9] J. Bahram and S. Fathpour, “Silicon Photonics,” *Journal of Lightwave Technology*, 24(12), pp. 4600-4615, Dec. 2006.
- [10] C. Lukas and M. Hochberg, “Silicon Photonics Design: From Devices to Systems,” Cambridge University Press, 2015.
- [11] Jinsoo Rhim, “Modeling, Design and Optimization of Si Photonic Transmitters,” Ph.D. dissertation, Dept. Elect. Eng., Yonsei Univ., Korea, 2015.
- [12] D. Lee, J. Han, G. Han, and S. M. Park, “10Gbit/s 0.0065 mm<sup>2</sup> 6mW analogue adaptive equaliser utilising negative capacitance,” *Electron. Lett.*, vol. 45, no. 17, pp.863–865, Aug. 2009.
- [13] S. Simon, G. Winzer, H. Rossmann, M. Kroh, L. Zimmermann, and T. Mausolf, “A PEDA approach for monolithic photonic BiCMOS technologies,” *SPIE Microtechnologies, International Society for Optics and Photonics*, 2015.
- [14] S. Kobayashi, Y. Yamamoto, M. Ito, and T. Kimura, “Direct frequency modulation in AlGaAs Semiconductor lasers,” *IEEE Journal of Quantum Electronics*, vol. 18, No. 4, pp. 582-575, Apr. 1982.
- [15] E. L. Wooten, K. M. Kissa, A. Yi-Yan, E. J. Murphy, D. A. Lafaw, P. F. Hallemeier, D. Maack, D. V. Attanasio, D. J. Fritz, G. J. McBrien, and D. E. Bossi, “A Review of Lithium Niobate Modulators for 132 Fiber-Optic Communications Systems,” *IEEE Journal of Selected Topics in Quantum Electronics*, vo. 6, No. 1, pp. 69-82, Jan./Feb. 2000.
- [16] G. V. Treyz, G. May, and J. –M. Halbout, “Silicon Optical Modulators at 1.3  $\mu\text{m}$  Based on Free-Carrier Absorption,” *IEEE Electron Device Letters*, vol. 12, No. 6, pp. 276-278, Jun. 1991.

- [17] L. Liao, A. Liu, D. Rubin, J. Basak, Y. Chetrit, H. Nguyen, R. Cohen, N. Izhaky, and M. Paniccia, "40 Gbit/s silicon optical modulator for high-speed applications," *Electronics Letters*, vo. 43, No. 22, pp. 1196-1197, Oct. 2007.
- [18] S. Gupta, S. A. Srinivasan, M. Pantouvaki, H. Chen, P. Verheyen, G. Lepage, D. Van Thourhout G. Roelkens, K. Saraswat, P. Absil, J. Van Campenhout," 50GHz Ge Waveguide Electro-Absorption Modulator Integrated in a 220nm SOI Photonics Platform," Optical Fiber Communication Conference (OFC), Tu2A.4, 2015
- [19] Q. Xu, B. Schmidt, J. Shakya, and M. Lipson, "Cascaded silicon micro-ring modulators for WDM optical interconnection," *Optics Express*, vol. 14, No.20, pp. 9431-9435, Oct. 2006.
- [20] K. Padmaraju and K. Bergman, "Resolving the thermal challenges for silicon microring resonator devices," *Nanophotonics*, vol. 3, Iss.4-5, pp. 269-281, Aug. 2014.
- [21] S. A. Srinivasan, M. Pantouvaki, S. Gupta, H. T. Chen, P. Verheyen, G. Lepage, G. Roelkens, K. Saraswat, D. V. Thourhout, P. Absil, and J. V. Campenhout, "56Gb/s Germanium Waveguide Electro-Absorption Modulator," *IEEE Journal of Lightwave Technology*, accepted for publication, 2015.
- [22] M. Streshinsky, R. Ding, Y. Liu, A. Novack, Y. Yang, Y. Ma, X. Tu, E. K. S. Chee, A. E. -J. Lim, P. G. -Q. Lo, T. Baehr-Jones, and M. Hochberg, "Low power 50 Gb/s silicon traveling wave Mach134 Zehnder modulator near 1300 nm," *Optics Express*, 21 (25), pp. 30350-30357, Dec. 2013.
- [23] X. Xiao, X. Li, H. Xu, Y. Hu, K. Xiong, Z. Li, T. Chu, J. Yu, and Y. Yu, "44-Gb/s Silicon Microring Modulators Based on Zigzag PN Junctions," *IEEE Photonics Technology Letters*, 24(19), pp. 1712- 1714, Oct. 2012.

- [24] R. Soref and B. Bennett, "Electrooptical effects in silicon", *IEEE J. Quantum Electron.*, vol. 23, no. 1, pp. 123-129, 1987.
- [25] H. A. Haus, "Coupling of modes -resonators and couplers," in *Waves and fields in optoelectronics*, Prentice-Hall, Inc. Englewood Cliffs New Jersey 07632, 1984
- [26] B. E. Little, S. T. Chu, H. A. Haus, J. S. Foresi, and J.-P. Laine, "Microring resonator channel dropping filter," *J. Lightwave Technol.*, vol. 15, pp. 998-1005, 1997
- [27] Reed, G. T. & Knights, A. P. *Silicon Photonics: An Introduction* Ch. 4, 97–103 (Wiley, 2004).
- [28] Qianfan Xu, Sasikanth Manipatruni, Brad Schmidt, Jagat Shakya, and Michal Lipson, "12.5 Gbit/s carrier-injection-based silicon micro-ring silicon modulators," *Opt. Express.*, vol.15, no.2,pp. 430-436, 2007
- [29] Jinsoo Rhim, Yoojin Ban, Byung-Min Yu, Jeong-Min Lee, and Woo-Young Choi, "Verilog-A behavioral model for resonance modulated silicon micro-ring modulator," *Opt. Express*, vol. 23, no. 7, pp. 8763-8772, 2015
- [30] Magdalena S. Nawrocka, Tao Liu, Xuan Wang and Roberto R. Panepucci, "Tunable silicon microring resonator with wide free spectral range," *Appl Phys Lett*, 89, 2006; Article ID: 071110.
- [31] B. J. Frey, D. B. Leviton, T. J. Madison, "Temperature-dependent refractive index of silicon and germanium," *Proc. SPIE*, Orlando, FL 2006, vol 6273, pp. 62732J-1 - 62732J-10
- [32] H. K. Tsang and Y. Liu, "Nonlinear optical properties of silicon waveguides," *Semicond. Sci. Technol*, vol 23, no 6,pp. 064007-1 - 064007-9, 2008
- [33] J. Leuthold, C. Koos and W. Freude, "Nonlinear silicon photonics," *nature photonics*, vol 4, pp 535-544, 2010

- [34] Q. Fang, J. Song, X. Luo, L. Jia, M. Yu, G. Lo, Y. Liu, “High Efficient Ring-Resonator Filter With NiSi Heater”, *IEEE Photon. Technol. Lett*, vol 24, no. 5, pp. 350-352, 2012
- [35] A. Arbabi and L. L. Goddard, “Measurements of the refractive indices and thermos-optic coefficients of  $\text{Si}_3\text{N}_4$  and  $\text{SiO}_x$  using microring resonances”, *Opt. Lett*, vol. 38, issue 19, pp.3878-3881, 2013
- [36] Y. Ban, B. M. Yu, J. Rhim, J. M. Lee and W. Y. Choi, “Modeling of self-heating effect for depletion-type Si micro-ring modulator,” *Optical Interconnects Conference (OIC), 2015 IEEE* [Online]Available: <http://ieeexplore.ieee.org/xpl/articleDetails.jsp?reload=true&number=7115722>
- [37] D. K. Schroder, R. N. Tomas, and J. C. Swartz, “Free Carrier Absorption in Silicon”, *IEEE J. Solid-State Circuits*, vol 13, (issue 1), pp. 180-187, 1978
- [38] W. D. Sacher and J. K. S. Poon, “Dynamics of microring resonator modulators,” *Opt. Express*, vol. 16, no. 20, pp. 15741-15753, 2008.
- [39] L. Zhang, Y. Li, J.-Y. Yang, M. Song, R. G. Beausoleil, and A. E. Willner, “Silicon-based microring resonator modulators for intensity modulation,” *IEEE J. Sel. Top. Quantum Electron.*, vol. 16, no. 1, pp. 149-158, 2010.
- [40] M. Song, L. Zhang, R. G. Beausoleil, and A. E. Willner, “Nonlinear distortion in a silicon microring-based electro-optic modulator for analog optical links,” *IEEE J. Sel. Top. Quantum Electron.*, vol. 16, no. 1, pp. 185-191, 2010.

- [41] Brian Pile, and Geoff Taylor, "Small-Signal Analysis of Microring Resonator Modulator," *Opt. Express*, vol. 22, no. 12, pp. 14913-14928, 2014.
- [42] Y. Ban, J.-M. Lee, B.-M. Yu, S.-H. Cho, and W.-Y. Choi, "Small-signal frequency responses for Si micro-ring modulator," *IEEE Optical Interconnects Conf.*, pp. 47-48, 2014.
- [43] J. Müller, F. Merget, S. Sharif Azadeh, J. Hauck, S. Romero García, B. Shen and J. Witzens, "Optical Peaking Enhancement in High-Speed Ring Modulators," *Scientific Reports*, vol. 4, no. 6310, pp. 1-9, 2014.
- [44] Samira Karimelahi and Ali Sheikholeslami, "Ring modulator small-signal response analysis based on pole-zero representation," *Opt. Express*, vol. 24, no. 7, pp. 7585-7599, 2016
- [45] Guoliang Li, Xuezhe Zheng, Jin Yao, Hiren Thacker, Ivan Shubin, Ying Luo, Kannan Raj, John E. Cunningham, and Ashok V. Krishnamoorthy, "25Gb/s 1V-driving CMOS ring modulator with integrated thermal tuning," *Opt. Express*, vol. 19, no. 21, pp. 20435-2443, 2011
- [46] A. Aktas and M. Ismail. "Pad de-embedding in RF CMOS," *IEEE Circuits Devices Mag.*, vol. 17, no. 3, pp.8-11, May 2001.
- [47] M. Pirola et al., "Multisectional modeling of high-speed electrooptic modulators integrated in a microwave circuit CAD environment," *J. Lightwave Technol*, vol. 21, no. 12, pp. 2989-2996, 2003.
- [48] F. Cappelluti et al., "Large-signal E/O modelling of traveling-wave electroabsorption modulators in an RF circuit CAD environment," *IEEE MTT-S Digest*, pp. 769-772, WE3C-3, 2004.
- [49] L. Zimmermann, D. J. Thomson, B. Boll, D. Knoll, S. Lischke, F. Y. Gardes, Y. Hu, G. T. Reed, H. Zimmermann, H. Porte,

“Monolithically Integrated 10Gbit/sec Silicon Modulator with Driver in 0.25 $\mu$ m SiGe:C BiCMOS,” *European Conference and Exhibition on Optical Communication (ECOC)* (The Institution of Engineering and Technology 2013), We.3.B.1.

## Abstract (In Korean)

# 자기 가열 현상을 고려한 공핍형 실리콘 마이크로 링 변조기 모델링

공핍형 실리콘 링 변조기에서 자기 가열현상이 정상 상태와 동적 상태 두가지 경우에 각각 어떻게 영향을 미치는지 연구하였다. 자기 가열현상은 도핑 된 링 도파관에 빛이 들어갔을 때 자유 반송자가 흡수 되면서 발생하며, 링 안의 유효 굴절률을 증가시켜서 공진 파장을 적색 이동 시키게 된다. 이러한 현상은 coupled-mode 이론에 의거하여 새로 제시된 자기 가열 상수,  $R$ 에 의해 모델링 되었다. 또한 새롭게 제시된  $R$  값이 마이크로 링 크기와 도핑의 정도에 따라 어떻게 변하는지 실험을 통해 경향성을 파악하였고 설명되었다. 또한, 이러한 정상 상태에서의 자기 가열 현상 모델을 기반으로 동적 상태에서 자기 가열 현상이 실리콘 링 변조기에 어떻게 영향을 주는지 분석하였다.

이 논문에서는 자기 가열 현상 모델링뿐만 아니라 공핍형 실리콘 링 변조기의 선형의 등가 회로 모델도 제시되었다. 이 등가회로 모델은 세가지로 나누어지며, 각각은 연결선과 패드

에 의한 기생 성분, PN 접합에서 생기는 전기적인 성분, 마지막으로 광의 소신호 모델을 나타내는 lossy한 LC 탱크이다. 제시된 이 등가 회로 모델을 통해, 실리콘 링 변조기의 주파수 특성을 분석할 수 있고, 변조기 구동 회로와의 연계 시뮬레이션을 통해 실리콘 포토닉 기반의 전체 송신기의 설계 최적화를 할 수 있다. 더 나아가 전압 의존적인 변수의 Verilog-A 모델링을 통해 실제 Large-signal의 등가회로 모델 또한 모델링 하였다. 제시된 각각의 모델들의 정확성은 모두 실험과의 비교를 통해 정확성이 확인되었다. 결과적으로, 이러한 모델들은 민감한 공핍형 실리콘 마이크로 링 변조기의 최적화 설계에 큰 도움이 될 것이다.

---

**핵심 단어:** 실리콘 포토닉스, 광 연결, 실리콘 마이크로 링 변조기, 자기가열 현상, 자기가열 상수, 등가회로 모델

## List of Publications

### *International Journal Papers*

- [1] **Myungjin Shin**, Yoojin Ban, Byung-Min Yu, Jinsoo Rhim, Lars Zimmermann, and Woo-Young Choi, “Parametric Characterization of Self-Heating in Depletion-Type Si Micro-Ring Modulators”. IEEE Journal of Selected Topics in Quantum Electronics (JSTQE), Vol. 22, No. 6, Article# 3400207 (2016).
- [2] **Myungjin Shin**, Yoojin Ban, Byung-Min Yu, Min-Hyeong Kim, Jinsoo Rhim, Lars Zimmermann and Woo-Young Choi, “A Linear Equivalent Circuit Model for Depletion-Type Silicon Micro-Ring Modulator”, accepted to Transactions on Electron Devices (TED)

## *International Conference Presentations*

- [1] Woo-Young Choi, **Myungjin Shin**, Jeong-Min Lee, Lars Zimmermann, “Equivalent Circuit Models for Silicon Photonics Devices,” Asia Communications and Photonics Conference (2016)
- [2] **Myungjin Shin**, Byung-Min Yu, Lars Zimmermann and Woo-Young Choi, “Parametric Characterization of Self-Heating in Si Micro-Ring Modulators”, 13th International Conference on Group IV Photonics,ThC6 (2016)

## ***Domestic Conference Presentations***

- [1] Byung-min Yu, **Myungjin Shin**, Lars Zimmermann, Woo-Young Choi, “Frequency Modulation Characteristics of High-Speed Si Micro-Ring Modulator”, The 23rd Conference on Optoelectronics and Optical Communications (Korea), pp.273-274 (2016)
- [2] **Myungjin Shin**, Byung-Min Yu, Yunsu Sung, Jinsoo Rhim and Woo-Young Choi, “Modeling of Self-Heating Effect in Depletion-Type Si Micro-Ring Modulator”, 2015 Photonics Conference (Korea), pp.252-253 (2015)
- [3] **Myungjin Shin**, Yoojin Ban, Byung-Min Yu, Yunsu Sung, and Woo-Young Choi, “Optimization of PN Junction Location for Si Micro-Ring Modulators”, Final Program of the Optical Society of Korea Summer Meeting 2015, T2D-V5 (2015)
- [4] Woo-Young Choi, Jinsoo Rhim, Byung-Min Yu, Yunsu Sung and **Myungjin Shin**, “Silicon Optical Modulators”, 2015 Photonics Conference (Korea), pp.474 (2015)
- [5] Minkyu Kim, **Myungjin Shin**, Tongsung Kim, and Woo-Young Choi, “Circuit-Level Modelling of 10-Gbps Si-Photonic Transceiver”, The 22nd Korean Conference on Semiconductors, pp.379 (2015).